Research Square

Preprints are preliminary reports that have not undergone peer review.
They should not be considered conclusive, used to inform clinical practice,
or referenced by the media as validated information.

LXRβ pathway suppresses CD8+ T cell activation in ovarian carcinoma ascites.

Magdalena Huber

magdalena.huber@staff.uni-marburg.de

University of Marburg https://orcid.org/0000-0002-2963-0693

Abdul Rahman Jouria

Philipps university of Marburg

Sonja Lieber

Philipps university of Marburg

Veronika Lutz

Philipps university of Marburg https://orcid.org/0000-0002-3139-0916

Hartmann Raifer

Philipps university of Marburg

Florian Finkernagel

Philipps University Marburg

Lena Kallenbach Kallenbach

Philipps university of Marburg

Andrea Nist

Philipps University Marburg

Thorsten Stiewe

Genomics Core Facility, Institute of Molecular Oncology, Member of the German Center for Lung Research (DZL), Philipps University Marburg https://orcid.org/0000-0003-0134-7826

Uwe Wagner

Philipps university of Marburg

Silke Reinartz

Philipps university of Marburg

Katrin Roth

Philipps university of Marburg

Michal Grzybek

TU Dresden Faculty of Medicine Carl Gustav Carus

Ünal Coskun

TU Dresden Faculty of Medicine Carl Gustav Carus

Cenk Gurdap

Karolinska Institutet https://orcid.org/0000-0002-5327-2523

Erdinc Sezgin
Karolinska Institute https://orcid.org/0000-0002-4915-388X
Jelena Pesek
Philipps university of Marburg
Verena Taudte
Insitute of Laboratory Medicine, Philipps University of Marburg
Bertram Bengsch
University of Freiburg
Laura Bierau
Philipps university of Marburg
Eva Herker
Philipps-Universität Marburg https://orcid.org/0000-0001-9644-2484
Anna Brichkina
Philipps University of Marburg https://orcid.org/0000-0001-8707-9900
Rolf Müller
https://orcid.org/0000-0003-3339-4248

Article

Keywords: Ovarian carcinoma, CD8+ T cells, cholesterol, LXRβ, TCR-signal transduction

Posted Date: November 4th, 2026

DOI: https://doi.org/10.21203/rs.3.rs-11364602/v1

License: This work is licensed under a Creative Commons Attribution 4.0 International License.
Read Full License

Additional Declarations: (Not answered)

LXRβ pathway suppresses CD8$^+$ T cell activation in ovarian carcinoma ascites.

Abdul Rahman Jouria[1], Sonja Lieber[1], Veronika Lutz[1], Hartmann Raifer[1,3], Florian Finkernagel[1,2], Lena Kallenbach[1], Andrea Nist[4], Thorsten Stiewe[5], Uwe Wagner[6], Silke Reinartz[2,6], Katrin Roth[2], Michal Grzybek[7], Ünal Coskun[7], Cenk Gurdap[8], Erdinc Sezgin[8], Jelena Pesek[9], Verena Taudte[9], Bertram Bengsch[10], Laura Bierau[11], Eva Herker[11], Anna Brichkina[1], Rolf Müller[2], Magdalena Huber[1]

[1]Institute of Systems Immunology, University of Marburg, 35043 Marburg, Germany

[2]Institute of Molecular Biology and Tumor Research, Center for Tumor Biology and Immunology, Philipps University, Marburg, Germany

[3]Core Facility Flow Cytometry, University of Marburg, 35043 Marburg, Germany

[4]Genomics Core Facility, Center for Tumor Biology and Immunology (ZTI), Philipps University, Marburg, Germany.

[5]Institute of Molecular Oncology, Philipps University, Marburg, Germany.

[6]Clinic for Gynecological Oncology and Gynecological Endocrinology, Center for Tumor Biology and Immunology (ZTI), Philipps University, Marburg, Germany

[7]Center of Membrane Biochemistry and Lipid Research TU Dresden Faculty of Medicine Carl Gustav Carus, Dresden, Germany

[8]CSI: Nano Lab, SciLifeLab, Karolinska Institute, Stockholm, Sweden.

[9]Translational Metabolomics, Core Facility Metabolomics, Department of Medicine, Philipps University Marburg, Marburg, Germany

[10]Department of Internal Medicine II, Gastroenterology, Hepatology, Endocrinology and Infectious Diseases, Medical Center, University of Freiburg, Faculty of Medicine, Freiburg, Germany

[11]Institute of Virology, University of Marburg, 35043 Marburg, Germany

Corresponding author: Prof. Magdalena Huber

Institute of Systems Immunology

Philipps-University of Marburg

Hans-Meerwein-Straße 3

35043 Marburg, Germany

Phone: +49(0)6421 - 2866818

E-mail: magdalena.huber@staff.uni-marburg.de

Running title: LXRβ limits $CD8^+$ T cell activation in ovarian carcinoma ascites

Key words**:** Ovarian carcinoma, $CD8^+$ T cells, cholesterol, LXRβ, TCR-signal transduction

ABSTRACT

Ovarian cancer (OC) is the deadliest gynecological malignancy, characterized by accumulating fluid (ascites) in the peritoneal cavity at the advanced stage. OC ascites exhibits immunosuppressive activity against various immune cells, including $CD8^+$ T cells, through mechanisms not yet fully understood. Here, we show that OC ascites suppresses sterol regulatory element-binding protein (SREBP)-driven genes crucial for cholesterol biosynthesis while inducing liver X receptor β (LXRβ) targets facilitating cholesterol elimination in $CD8^+$ T cells. This transcriptional reprogramming was accompanied by a failure to remodel the lipidome toward membrane-supportive phospholipids, promote free cholesterol accumulation, and increase plasma membrane order following T cell receptor (TCR) engagement. These defects coincided with blunted proximal TCR signal transduction, impaired TCR surface recycling, and reduced induction of the transcription factor Interferon Regulatory Factor 4 (IRF4), resulting in diminished $CD8^+$ T cell activation and function. Targeted lipidomics identified enrichment of 27-hydroxycholesterol (27-HC) in OC ascites relative to non-malignant ascites. Adding 27-HC to the culture media recapitulated the suppressive phenotype and the associated SREBP/LXR transcriptional signature, suggesting that the 27-HC/LXR axis contributes to OC ascites-mediated $CD8^+$ T cell suppression. Accordingly, pharmacological inhibition of LXRβ with the inverse agonist SR9243 partially restored $CD8^+$ T cell activity and IRF4 expression in OC ascites. In turn, pharmacological activation of LXRβ with the agonist GW3965 phenocopied the suppression induced by OC ascites. These findings link OC ascites to impaired membrane order and TCR signaling in $CD8^+$ T cells via a 27-HC/LXRβ axis, suggesting LXRβ antagonism may restore antitumor $CD8^+$ T cell function in OC.

INTRODUCTION

Ovarian cancer (OC) is the deadliest gynecological malignancy, with more than 295,000 new diagnoses and 184,000 deaths worldwide each year[1]. High-grade serous carcinoma (HGSC), the most common histotype, accounts for 70-80% of OC-related deaths[2]. Advanced-stage disease is frequently accompanied by malignancy-associated ascites, a cellularly and biochemically complex compartment that promotes tumor progression[3,4] through mechanisms such as tumor-associated vascular hyperpermeability and impaired peritoneal fluid clearance[5]. Ascites-derived lipids, including lysophosphatidic acid and arachidonic acid[6–8] contribute to this pro-tumorigenic environment. Furthermore, cholesterol content is elevated in malignant ascites relative to non-malignant ascites[9,10], consistent with the increased cholesterol and fatty acid biosynthesis characteristic of OC tumor cells[11].

$CD8^+$ T cells are central mediators of antitumor immunity[12], yet chronic antigen exposure within the tumor microenvironment can drive a progressive loss of effector function[13–15], resulting in distinct subsets of exhausted $CD8^+$ T cells that differentially retain tumor-control capacity and responsiveness to cytotoxic T-lymphocyte-associated protein 4 (CTLA-4) and programmed cell death protein 1 (PD1) checkpoint blockade[16]. While $CD8^+$ T cell infiltration correlates with improved OC survival[17–19], checkpoint inhibitor efficacy remains limited[20–22], indicating that mechanisms beyond checkpoint engagement restrain cytotoxic T-lymphocyte (CTL) function in OC. Accordingly, our group has shown that OC ascites suppresses T cell receptor (TCR)-induced NF-κB and NFAT signaling in T cells, and that ascites-resident $CD8^+$ T cell accumulation and function are linked to clinical outcome[23–25].

Cholesterol and membrane lipid composition are increasingly recognized as critical regulators of T cell activation by controlling membrane organization, TCR clustering, and downstream signaling events[26]. Cholesterol binds the TCR-CD3 complex to set a biophysical threshold for receptor triggering[27], and membrane cholesterol availability is actively regulated during TCR engagement via non-vesicular sterol transport[28], with downstream signal strength transduced through a network of transcription factors including the Interferon Regulatory Factor 4 (IRF4)[29–31]. Cellular cholesterol content is governed by the reciprocal sterol regulatory element-binding protein (SREBP) – liver X receptor (LXR) axis[32,33], and LXRβ, the dominant LXR isoform in T cells, constrains T cell fitness upon activation[34]. In breast cancer, the oxysterol 27-hydroxycholesterol (27-HC) suppresses SREBP2 and activates LXR in intratumoral T cells,

thereby impairing their antitumor cytotoxicity[35] and altering immune cell populations that facilitate metastatic progression[36].

Whether OC ascites-derived oxysterols engage the SREBP/LXRβ axis to disrupt $CD8^+$ T cell membrane order and TCR-proximal signaling remains to be defined. Here, we show that OC ascites suppresses SREBP-target cholesterol biosynthetic genes while inducing LXR-dependent transcripts in $CD8^+$ T cells, accompanied by loss of membrane remodeling and blunted TCR signal transduction. We identify 27-HC as an ascites-enriched oxysterol that engages the LXRβ axis and drives $CD8^+$ T cell suppression *in vitro*.

RESULTS

OC ascites suppresses TCR-driven activation and function of CD8$^+$ T cells

To investigate the suppressive capacity of OC ascites on CD8$^+$ T cell activation, we established a short-term TCR stimulation protocol. CD8$^+$ T cells isolated from peripheral blood mononuclear cells (PBMCs) of healthy donors (HD) were stimulated with anti CD2/CD3/CD28 coated beads (TAE beads) in the presence of cell-free pooled OC ascites, pooled liver cirrhosis ascites (LC ascites) acting as a non-malignant control, or RPMI medium. After 16 hours of primary stimulation, surface expression of the TCR activation markers (CD69, CD25)[37,38] was measured. To evaluate effector function, we analyzed cells for the effector cytokines TNF and IFN-γ, as well as the degranulation marker CD107a. Proliferative capacity was evaluated after five days of culture (Fig. 1A). CD8$^+$ T cells activated in the presence of OC ascites exhibited significantly reduced frequencies of CD25 and CD69 compared to RPMI control, with a similar trend relative to LC ascites, and without a corresponding reduction in cell viability (Figs. 1B, S1A, B). Consistent with impaired activation, cells exposed to OC ascites showed significantly diminished TNF and IFN-γ production and reduced CD107a surface mobilization relative to controls (Figs. 1C, 1D). Furthermore, CD8$^+$ T cell proliferation was markedly reduced under the OC ascites treatment (Fig. 1E).

To assess whether these *ex vivo* findings reflected the *in vivo* state of tumor-infiltrating lymphocytes, we next analyzed CD8$^+$ T cells isolated directly from OC ascites and compared them with CD8$^+$ T cells isolated from HD PBMCs. We isolated OC ascites-resident CD8$^+$ T cells and assessed TNF, IFN-γ, and CD107a expression, as well as proliferative capacity (Fig. 1F, S1C). Compared with HD CD8$^+$ T cells, OC ascites-derived CD8$^+$ T cells showed significantly reduced effector cytokine production, degranulation, and proliferation upon stimulation (Figs. 1G-I).

Collectively, the similarity between the *ex vivo* suppression model and the functional impairment observed in ascites-resident CD8$^+$ T cells in OC patients suggests that the ascites microenvironment contributes to CD8$^+$ T cell dysfunction *in vivo* (Fig. S1D).

OC ascites reprograms the SREBP/LXRβ pathways and co-regulates TCR signaling gene expression in CD8$^+$ T cells.

To identify the transcriptional mechanisms underlying OC ascites-mediated $CD8^+$ T cell suppression, we performed bulk RNA sequencing (RNA-seq) on $CD8^+$ T cells from HD activated in the presence of OC ascites (n = 41 independent patient ascites samples) or RPMI medium (n = 12) (Fig. S2A). Uniform Manifold Approximation and Projection (UMAP) dimensionality reduction revealed a transcriptional state clearly separated from medium controls in $CD8^+$ T cells cultured in OC ascites (Fig. 2A), indicating that OC ascites induces a coherent transcriptional reprogramming across the entire patient cohort. Differential expression analysis identified 141 genes meeting the significance threshold ($log_2FC > 1$, FDR ≤ 0.1), 108 downregulated and 33 upregulated in OC ascites relative to control cells (Fig. S2B). Hierarchical clustering of these differentially expressed genes (DEGs) revealed three transcriptionally distinct modules, with module 1 showing consistent downregulation across all OC ascites samples compared to RPMI controls (Fig. 2B).

Unsupervised clustering resolved DEG into three transcriptional modules with distinct gene ontology (GO) enrichments (Fig. 2C). Module 1 comprises transcripts uniformly downregulated across all 41 OC ascites samples and was enriched for two functionally related gene sets: (i) SREBP-regulated cholesterol and fatty acid biosynthesis genes, including *ACAT2*, *HMGCS1*, *HMGCR*, *IDI1*, *FDFT1*, *SQLE*, *CYP51A1*, *DHCR7*, *DHCR24*, and *INSIG1*[26,27], consistent with the requirement for SREBP-driven metabolic programming in effector T cell differentiation[39] (Fig. S2C); and (ii) TCR signaling targets, *NR4A1*, *IL21R*, *REL*, *TNFRSF4,* including the transcription factor (TF) *IRF4*[40–42]. Module 2 was enriched for DNA metabolic processes, while module 3 was enriched for markers associated with a pre-dysfunctional state, including *GZMK*, *EOMES,* and *CXCR4*[43], as well as type I interferon signaling genes. Unlike module 1, the transcriptional changes in modules 2 and 3 were not uniformly shared across all OC ascites samples.

Given the significant suppression of module 1 transcripts across all 41 ascites samples, we focused on it to identify a shared suppressive mechanism. This module was enriched for both SREBP pathway targets and TCR signaling genes; therefore, we examined whether their expression was coordinately regulated. Distance correlation analysis of the RNA-seq dataset from OC ascites cultured cells revealed strong co-expression among lipid metabolic genes (*FASN*, *HMGCR*) and TCR-downstream targets, including *IRF4* (Fig. 2D). In contrast, two LXR target genes, namely *MYLIP* encoding an inducible degrader of the LDL receptor and *SREBF1*

encoding SREBP1[44] showed expression patterns inversely correlated with TCR targets. Pearson correlation analysis confirmed that SREBP targets *FASN* (R = 0.76, $p<0.01$) and *HMGCR* (R = 0.68, $p<0.01$) correlated positively with *IRF4* expression across OC ascites samples, while the LXR target *MYLIP* correlated negatively (R = -0.67, $p<0.01$) (Fig. 2E). A consistent yet weaker correlation was also observed in $CD8^+$ T cells activated in RPMI medium (FASN: R = 0.64; HMGCR: R = 0.56; MYLIP: R = -0.52; all p<0.01) (Fig. S2D), indicating that this transcriptional coupling reflects a general feature of $CD8^+$ T cell activation.

Since SREBP target genes were uniformly suppressed while LXR-dependent transcripts were induced, we reasoned that elevated exogenous cholesterol in OC ascites might drive this pattern through negative feedback suppression of SREBP activity[26,32]. Analysis of published bulk RNA sequencing data[45] revealed that OC tumor cells expressed higher levels of cholesterol biosynthesis genes compared to tumor-associated macrophages or tumor-infiltrating lymphocytes (Fig. S2E), and macrophage-derived oxysterols have been shown to shape local immune-cell inflammatory features[46]. This suggests that tumor cells, and likely macrophages, may drive the increased lipid content in OC ascites.

To validate the RNA-seq findings at the transcript level and confirm specificity relative to a non-malignant ascites control, RT-qPCR was performed on $CD8^+$ T cells activated in RPMI, LC ascites, and OC ascites (Fig. 2F). Consistent with RNA-seq data, *IRF4*, *HMGCR,* and *SQLE* mRNA levels were significantly reduced in OC ascites-cultured $CD8^+$ T cells compared to both control conditions. In contrast, the LXR target genes *ABCA1, ABCG1,* and *MYLIP* were significantly upregulated in $CD8^+$ T cells cultured in OC ascites, with LC ascites showing intermediate or control-level expression, consistent with coordinated activation of the cholesterol efflux pathway described in other chronically lipid-exposed immune contexts[47]. These results confirmed the RNA-Seq data on dysregulated SREBP/LXRβ pathway and TCR signaling gene expression in $CD8^+$ T cells activated in OC ascites.

OC ascites suppresses TCR-driven signal transduction and TCR trafficking

Transcriptomic profiling identified *IRF4* as one of the most significantly downregulated TF in $CD8^+$ T cells activated in OC ascites relative to RPMI medium (Fig. 2B, F). To confirm this at the protein level, we measured IRF4 expression by intracellular flow cytometry. IRF4 protein was

significantly reduced in $CD8^+$ T cells cultured in OC ascites compared to RPMI medium, while cells cultured in LC ascites exhibited an intermediate reduction, suggesting that IRF4 suppression is at least partly specific to the OC ascites microenvironment (Fig. 3A). To assess the functional consequences of reduced IRF4 levels in human $CD8^+$ T cells, we performed siRNA-mediated knockdown, which achieved robust downregulation of IRF4 protein without affecting cell viability (Fig. 3B, S3A, B). $CD8^+$ T cells treated with siRNA against IRF4 exhibited significantly reduced proliferation and a marked decrease in $CD25^+CD69^+$ double-positive cells following TCR stimulation compared to scrambled (scr) siRNA (Fig. 3C, D), demonstrating that IRF4 is required for TCR-driven activation and proliferation in human $CD8^+$ T cells. Together, these findings indicate that the suppression of IRF4 expression by OC ascites likely contributes to impaired $CD8^+$ T cell activation in the OC microenvironment.

In addition to *IRF4*, RNA-Seq analysis revealed broad downregulation of TCR target genes in $CD8^+$ T cells activated in OC ascites, pointing to generalized suppression of TCR signal transduction. To functionally interrogate the proximal TCR signaling cascade[27,37,38,48], we performed time-resolved phosphorylation analysis of key signaling intermediates following anti-CD3/CD28 stimulation in OC ascites versus RPMI (Fig. 3E). Cells activated in OC ascites exhibited significantly blunted phosphorylation of Lck (Tyr394), ZAP70 (pY292), PLCγ1 (pY783), ERK1/2 (pT202/pY204) (Fig. 3F). Taken together, these data demonstrate that OC ascites suppresses proximal TCR signal transduction in $CD8^+$ T cells.

TCR activation triggers receptor internalization, followed by intracellular sorting and subsequent recycling to the plasma membrane, a process whose efficiency depends on the strength of the preceding TCR signal[49]. To assess whether the TCR-signaling impairment observed in OC ascites is accompanied by altered TCR surface dynamics, we tracked surface TCR α/β expression (Fig. 3G). In both conditions (OC ascites and RPMI), TCR surface levels declined upon activation, consistent with activation-induced internalization. Cells activated in RPMI progressively recovered surface TCRα/β expression during the resting phase, reaching significantly higher levels by 24 hours; cells activated in OC ascites showed diminished TCR surface re-expression. These findings indicate that OC ascites impairs surface TCR recovery, likely due to reduced signaling-dependent TCR recycling.

Taken together, OC ascites suppresses TCR-mediated signaling and TCR recycling, thereby impairing $CD8^+$ T cell activation.

OC ascites alters lipid remodeling and promotes lipid droplet generation.

Transcriptional dysregulation of the SREBP/LXR axis suggested altered intracellular lipid homeostasis in $CD8^+$ T cells exposed to OC ascites. To directly test this, we performed untargeted lipidomics on $CD8^+$ T cells cultured in RPMI medium or OC ascites, with or without TCR activation (Fig. S4A). Unsupervised clustering identified three lipid modules with distinct regulation patterns (Fig. 4A, Table S6). Lipids in Module 1 and Module 2 were dynamically regulated by TCR activation in RPMI-cultured $CD8^+$ T cells, whereas lipids in Module 3 were elevated specifically in OC ascites-cultured $CD8^+$ T cells independent of activation status.

In RPMI, TCR activation induced a coordinated shift in the lipidome (Fig. 4B), with downregulation of neutral lipid species including cholesteryl esters (CE) and triglycerides (TG), the principal constituents of lipid droplets (LD)[50,51] and upregulation of polar membrane lipids, including phosphatidylcholines (PC), phosphatidylethanolamines (PE), and diacylglycerols (DAG). Given that PC and PE are core determinants of membrane fluidity, and that DAG is a direct second messenger downstream of TCR-proximal signaling[52], this shift is consistent with a transition from lipid storage to lipids that support membrane remodeling and signal transduction during activation.

This activation-induced shift in the lipidome was absent in OC ascites. Direct comparison of ascites-activated versus RPMI-activated $CD8^+$ T cells (Fig. 4C) showed that ascites-cultured cells failed to downregulate neutral lipids and instead accumulated a broad range of CE species e.g., CE (16:0), CE (16:1), CE (18:1), CE (20:1), and TG species. Several of these lipid species showed significantly higher fold-changes than the PC/PE species that dominated the RPMI-activation signature. Principal component analysis (PCA) (Fig. 4D) confirmed this pattern at the global lipidome level: RPMI-activated and RPMI-non-activated cells separated clearly along PC1, whereas ascites-activated and ascites-non-activated cells overlapped substantially, indicating that TCR activation is not linked to lipidome remodeling in ascites-exposed $CD8^+$ T cells. Consistent with this, PCA separated RPMI-activated and ascites-activated cells, underscoring that OC ascites exposure is the dominant determinant of lipidomic identity under TCR-activation conditions.

To determine whether OC ascites itself could supply these lipids, we performed lipidomics on OC ascites fluid (Fig. S4B, Table S7). OC ascites was strongly enriched relative to

RPMI in both neutral lipids (CE, TG) and polar lipids (PC), with CE (22:4), PC (42:7), and PC (O-40:2) showing the largest enrichment (>100-fold relative to RPMI for the top species). This is consistent with the neutral lipid accumulation observed in OC ascites-cultured $CD8^+$ T cells, suggesting probable uptake of exogenous lipids from the OC ascites microenvironment.

Given the CE and TG accumulation detected by lipidomics, we used Nile Red staining to directly assess LD content. $CD8^+$ T cells cultured in OC ascites showed a significant increase in LDs per cell (mean RPMI vs OC ascites LDs per cell, Fig. 4E), consistent with the neutral lipid accumulation detected by lipidomics. We next asked whether *de novo* synthesis of CE or TG contributes functionally to the suppression of $CD8^+$ T cell activation in OC ascites. Inhibition of Sterol O-acyltransferase 1 (SOAT1), which catalyzes CE synthesis, with the inhibitor K-604 caused only a modest increase in $CD69^+/CD25^+$ frequency in OC ascites-cultured cells. This increase was statistically significant at 10 μM compared with RPMI-cultured controls (Fig. S4C), indicating a partial contribution. Inhibition of TG synthesis via Diacylglycerol-O-Acyltransferase (DGAT1, DGAT2), or triacsin C, which blocks fatty acid activation prior to esterification into TG or CE, did not alter $CD8^+$ T cell activation in either RPMI or OC ascites (Fig. S4D). These results indicate that *de novo* CE and TG synthesis are not major contributors to OC ascites-induced suppression of $CD8^+$ T cell activation, despite the increased LD content in OC ascites-cultured $CD8^+$ T cells.

Overall, OC ascites disrupts $CD8^+$ T cell lipid homeostasis and prevents the TCR activation-associated shift toward membrane and signaling-competent phospholipids. However, the resulting accumulation of CE and TG does not appear mechanistically required for suppression of activation, suggesting that the functional consequences of OC ascites exposure operate through a pathway distinct from CE/TG storage.

OC ascites alters plasma membrane order and restricts intracellular cholesterol accumulation in $CD8^+$ T cells

We next considered mechanisms by which OC-driven disruption of lipid homeostasis might restrict $CD8^+$ T cell activation and TCR signal transduction. OC ascites is enriched in multiple lipid classes including CE, TG, FA and phospholipids (Fig. S4B), suggesting that its lipid composition may directly influence T cell membrane biology. T cell activation induces lipid

remodeling and elevates cholesterol content in the plasma membrane, thereby increasing membrane order, which is important for efficient TCR signal transduction[52]. Given the reduced transcription of cholesterol synthesis enzymes and the impaired lipid remodeling following TCR activation in $CD8^+$ T cells cultured in OC ascites, we hypothesized that membrane order might be altered. Thus, we analyzed membrane order in $CD8^+$ T cells activated in ascites or RPMI using the solvatochromic membrane probe Pro12A, applying generalized-polarization-based membrane order quantification, as previously validated for related solvatochromic probes[53]. The generalized polarization parameter (GP) quantifies the probe's spectral shift. Large shifts result in low GP values and correlate with increased membrane fluidity, indicating lower lipid order and decreased lipid packing[54] (Fig. 5A). Interestingly, activation of $CD8^+$ T cells via TCR increased membrane order (Fig. 5B, C), which was consistent with the general lipid remodeling after $CD8^+$ T cell activation in RPMI (Fig. 4A, B). In contrast, $CD8^+$ T cell activation in OC ascites did not change membrane order, confirming the loss of lipid remodeling revealed by lipidomics. Thus, $CD8^+$ T cells activated in ascites display lower membrane order than those activated in RPMI. Given that membrane order plays a key role in $CD8^+$ T cell activation[55], these data suggest a potential mechanism underlying impaired $CD8^+$ T cell activation in OC ascites.

Since we detected decreased membrane order, which can be caused by lower cholesterol content, we next analyzed intracellular free cholesterol levels in $CD8^+$ T cells activated via TCR in ascites or RPMI using Filipin III staining (Fig. 5D). $CD8^+$ T cells activated in RPMI showed a significant increase in free cholesterol compared to non-activated cells, consistent with the cholesterol accumulation expected during T cell activation. Interestingly, $CD8^+$ T cells activated in OC ascites showed reduced free cholesterol levels compared with RPMI-activated cells and did not exhibit the activation-induced increase in free cholesterol. This is notable, as OC ascites is itself highly enriched in CE, suggesting that cholesterol acquired from the OC ascites microenvironment is stored within LDs rather than entering the membrane-accessible free cholesterol pool.

To establish whether a lipid fraction of OC ascites was causally responsible for these effects, we supplemented RPMI with individual lipid classes, including cholesterol, GM3 ganglioside, polyunsaturated fatty acids (PUFAs), and a lipid mixture (Fig. S5A). Notably, GM3 ganglioside, PUFAs, and the lipid mixture did not significantly affect $CD8^+$ T cell activation or

viability. Cholesterol supplementation, however, reduced $CD8^+$ T cell activation in a dose-dependent manner, mirroring the suppressive phenotype observed in OC ascites. Notably, this reduction in activation was evident at 10 μg/ml cholesterol, a concentration that did not impair T cell viability, indicating that cholesterol restricts $CD8^+$ T cell activation independently of cytotoxic effects. However, at the highest concentration tested, cell viability declined substantially, indicating that toxicity contributes to reduced activation at this dose. Because $CD8^+$ T cells cultured in OC ascites did not show reduced viability despite reduced activation, we speculated that ascites-induced suppression of $CD8^+$ T cell activation occurs through additional mechanisms.

Taken together, these findings indicate that impaired free cholesterol accumulation and membrane order contribute to OC ascites-induced $CD8^+$ T cell dysfunction, as measured by impaired TCR-proximal signal transduction and diminished proliferation and effector function. Cholesterol dysregulation alone did not fully recapitulate the ascites phenotype, suggesting that other ascites-derived factors likely act in concert. High ascites cholesterol content is associated with both suppression of cholesterol biosynthesis genes (Fig. 2) and accumulation of cholesteryl esters within LD (Fig. 4). However, inhibiting CE synthesis did not restore $CD8^+$ T cell activation (Fig. S4D). Therefore, LD formation is unlikely to account for the reduced membrane order. Thus, we postulate that suppressing cholesterol biosynthesis is linked to the loss of activation-induced free cholesterol upregulation (Fig. 5D) and, consequently, to decreased membrane order.

OC ascites impairs $CD8^+$ T cell activation through the 27-HC/LXRβ signaling axis

Although OC ascites drives broad lipid metabolic reprogramming and TCR signaling defects in $CD8^+$ T cells, the contribution of its lipid fraction to these immunosuppressive effects remained unclear. We therefore depleted OC ascites of its lipids using the CleanAscite delipidation reagent and assessed $CD8^+$ T cell activation across three conditions: RPMI, whole OC ascites, and delipidated ascites (Fig. 6A, S6A). Delipidation of OC ascites restored $CD8^+$ T cell activation to levels detected in RPMI, indicating that the lipid fraction of OC ascites is necessary and sufficient to drive suppression of $CD8^+$ T cell activation. Consistently, delipidation restored $TNF^+IFN\text{-}\gamma^+$ polyfunctional cytokine production (Fig. S6B) and IRF4 expression (Fig. S6C) to levels detected in RPMI controls.

We next sought to identify suppressive lipid species in OC ascites. Because 27-HC has been reported to inhibit human CAR T cell activation[35], we quantified this oxysterol by targeted mass spectrometry across OC and LC ascites (Fig. 6B and Table S8). 27-HC was significantly elevated in OC ascites relative to LC ascites, identifying it as an oxysterol enriched in the immunosuppressive lipid compartment of OC ascites. This is consistent with the described features of 27-HC as a broadly bioactive, endogenously abundant oxysterol that can modulate LXRβ signaling at physiological concentrations[56]. Therefore, we hypothesized that the 27-HC/LXRβ signaling axis might mediate lipid-driven suppression of $CD8^+$ T cells in OC ascites.

To test whether 27-HC alone can drive LXRβ-mediated T cell suppression independent of other ascites components, we treated $CD8^+$ T cells with exogenous 27-HC (10 μM; non-cytotoxic; Fig. S6D). 27-HC significantly reduced $CD25^+CD69^+$ activation frequencies relative to vehicle-treated controls (Fig. 6C) and upregulated *ABCG1*, *MYLIP*, and the LXR-induced SREBP pathway gene *SREBF1*, while simultaneously suppressing the SREBP2-target genes *HMGCR* and *SQLE* (Fig. 6D). 27-HC also significantly decreased TNF production (Fig. S6E) and CD107a surface expression (Fig. S6F). These data establish that 27-HC is sufficient to activate LXRβ signaling and suppress $CD8^+$ T cell activation, identifying the 27-HC/LXRβ axis as one mechanistic pathway linking the suppressive lipid compartment of OC ascites to $CD8^+$ T cell dysfunction.

To test whether LXRβ activation alone can phenocopy OC ascites-mediated suppression, we treated $CD8^+$ T cells with the synthetic LXR agonist GW3965 (2 μM) during TAE bead stimulation in RPMI. GW3965 significantly reduced $CD25^+CD69^+$ activation frequencies relative to vehicle-treated controls (Fig. S6G) and upregulated the canonical LXR target genes *ABCG1* and *MYLIP,* and the LXR-induced SREBP pathway gene *SREBF1* (Fig. S6H), recapitulating the transcriptional signature observed in OC ascites-exposed T cells (Fig. 2) and corroborating the effects of endogenous 27-HC. These data demonstrate that LXRβ agonist alone is sufficient to suppress TCR-driven $CD8^+$ T cell activation.

We then asked whether LXRβ signaling is functionally required for suppression within the OC ascites microenvironment. We treated $CD8^+$ T cells with the LXRβ inverse agonist SR9243 (50 μM, non-cytotoxic; Fig. S6I) during activation in OC ascites. This higher concentration reflects the lipid-sequestering capacity of OC ascites, which reduces the

effective availability of free drug compared with standard culture conditions. SR9243 significantly increased both $CD69^{+}CD25^{-}$ and $CD25^{+}CD69^{+}$ activation frequencies (Fig. 6E). Consistent with improved T cell activation, SR9243 also significantly increased the production of the effector cytokines TNF and IFN-γ (Fig. 6F). SR9243 significantly increased intracellular IRF4 protein expression (Fig. 6G). However, the partial rescue indicates that the suppressive lipid compartment of OC ascites contains additional immunomodulatory species beyond 27-HC, including cholesterol, that additionally contribute to $CD8^{+}$ T cell dysfunction.

Collectively, these findings identify 27-HC as an oxysterol enriched within the lipid fraction of OC ascites, sufficient to activate LXRβ signaling and suppress $CD8^{+}$ T cell activation. Pharmacological activation of LXRβ mimics this suppression, while blocking LXRβ partially restores activation, IRF4 expression, and effector cytokine production in OC ascites. This suggests that the LXRβ signaling pathway contributes to this suppression. We therefore propose that 27-HC-driven LXRβ activation impairs $CD8^{+}$ T cell activation and antitumor immunity in OC.

DSICUSSION

This study identifies 27-HC as a key mediator linking the OC ascites microenvironment[7,9] to $CD8^+$ T cell dysfunction. Building on our prior findings that OC ascites restricts TCR-proximal NF-κB and NFAT signaling[24] and that $CD8^+$ T-cell accumulation and function in OC ascites are linked to clinical outcomes[23], we show that OC ascites suppresses SREBP-dependent cholesterol biosynthesis genes while inducing LXR-targets in $CD8^+$ T cells. This transcriptional signature is associated with impaired TCR-proximal signal transduction, reduced membrane order, and diminished effector function. Pharmacological LXRβ agonism reproduced this suppressive phenotype; LXRβ antagonism partially reversed it in OC ascites, and adding exogenous 27-HC to RPMI recapitulated the transcriptional signature and the functional defect of $CD8^+$ T cells activated in OC ascites. Together with the selective enrichment of 27-HC in OC relative to LC ascites, these data support a model in which tumor-derived cholesterol[7,9,10] both directly engage SREBP cleavage-activating protein (SCAP)-mediated feedback inhibition of its own synthesis and may fuel local 27-HC production, which serves as an endogenous LXRβ ligand. Together, these mechanisms restrain SREBP2-dependent cholesterol synthesis and TCR signaling competence. This reframes OC ascites-induced $CD8^+$ T cell suppression not as checkpoint-derived exhaustion[13–15] or as nutrient competition, but as sterol-sensing-dependent dysfunction.

Mechanistically, our data directly support the conclusion that 27-HC engages the canonical SREBP, SCAP, and insulin-induced gene (INSIG) axis: exogenous 27-HC alone was sufficient to suppress transcription of the key cholesterol synthesis genes *HMGCR* and *SQLE*, demonstrating that the oxysterol reproduces not only LXR-target gene induction but also induction of SREBP-dependent genes detected in transcriptional module 1 (Fig. 2B). Under sterol-sufficient conditions, oxysterols bind INSIG and stabilize the SCAP-INSIG complex in the endoplasmic reticulum (ER), preventing SCAP-mediated escort of SREBP2 to the Golgi, where sequential proteolytic cleavage releases the transcriptionally active nuclear fragment[57]. Retaining SREBP2 in its inactive ER-bound form would explain the uniform downregulation observed across transcriptional module 1, including *HMGCR, SQLE,* and *IDI1* (Fig. 2B, S2C), since this spans the mevalonate-to-cholesterol pathway rather than a single rate-limiting step[32,33]. In parallel, 27-HC acts directly as an endogenous LXR ligand[44], and we observed consistent induction of the LXR-dependent genes *ABCA1, ABCG1, and MYLIP*. MYLIP-mediated degradation of the LDL receptor would further restrict exogenous cholesterol uptake, thereby

increasing SREBP2-driven biosynthetic shutdown. The inverse correlation between SREBP2 targets (*FASN, HMGCR*) and *MYLIP*, and their shared relationship to *IRF4*, suggests a reciprocal connection, consistent with the SREBP-LXR regulatory loop described in hepatocytes and macrophages[58]. We extend this concept to OC-ascites-conditioned $CD8^+$ T cells. This interpretation aligns with the link between TCR-proximal signal strength and IRF4 induction[37,38], as well as with topography-based models of TCR-proximal signalosome assembly in which membrane organization itself influences signal propagation[59]. Together, our data indicate a connection between sterol pathway suppression and impaired TCR-driven activation, proliferation, and cytokine production in $CD8^+$ T cells.

Beyond transcriptional suppression of biosynthetic enzymes, our functional data indicate that 27-HC/LXRβ signaling affects the physical properties of the $CD8^+$ T cell plasma membrane. Reduced free cholesterol accumulation upon activation, together with failure to remodel the lipidome toward membrane-supportive phospholipids, led to decreased membrane order and consequently impaired phosphorylation of Lck, ZAP70, PLCγ1, and ERK1/2. This effect is consistent with direct cholesterol-driven $CD8^+$ T cell exhaustion described in other tumors[60]. Impaired membrane order as a suppressive mechanism of OC ascites is not unique to $CD8^+$ T cells, since OC-ascites-derived arachidonic acid likewise perturbs lipid raft structure to impair JAK-STAT signaling in macrophages[6,7]. Furthermore, polar lipid uptake via the scavenger receptor class B type 1 (SR-B1) disrupts membrane order in OC-ascites-exposed natural killer (NK) cells[61]. Notably, these three mechanisms reduce membrane order through distinct pathways: exogenous lipid uptake (in NK cells and macrophages) and impaired endogenous biosynthesis (as presented for $CD8^+$ T cells), both of which are consistent with the differential reliance on lipid metabolic salvage versus synthesis observed across chronically activated or inflamed T cell populations[62]. This also indicates that different OC ascites-resident immune populations can reach the same biophysical endpoint, albeit through mechanistically non-redundant routes. Our data are in agreement that T cell metabolic and functional fate are tightly interlinked within a given microenvironment[63]. These implications could inform new therapeutic options, since uptake-driven and biosynthesis-driven membrane disorder would respond to different interventions (transporter blockade versus LXRβ antagonism, respectively).

Our data also extend the description of cholesterol as a direct, TCR-intrinsic regulator of receptor triggering[27,28] and LXR-mediated suppression of T cell fitness[34]. Furthermore, we expand knowledge of 27-HC/LXR signaling, which impairs $CD8^+$ T cell metabolic fitness broadly across solid tumors[35], by linking 27-HC/LXR action to defects in membrane biophysical properties and, thereby, to TCR-proximal signaling. We also show that OC ascites itself is a quantifiable oxysterol reservoir. Our data agree with the characterization of 27-HC as a bioactive, immune-cell-modulating metabolite[36] and with its capacity to restrain cholesterol synthesis to influence immune cell activation[64].

Our experiments with delipidated OC ascites, in which a reduction in lipid content was sufficient to restore $CD8^+$ T cell activation, and with the LXRβ inverse agonist SR9243, which produced only a partial rescue, indicate that 27-HC/LXRβ signaling is one of the lipid-dependent suppressive axes in OC ascites resulting in membrane-order disruption as recently described[65].

Collectively, our findings position 27-HC as a mechanistic link between cholesterol-rich OC ascites and impaired $CD8^+$ TCR signaling, acting through coordinated suppression of SREBP2-driven cholesterol biosynthesis and LXRβ-driven membrane remodeling programs. This oxysterol/LXRβ axis operates alongside, rather than in place of, established checkpoint-receptor[19–21] and polar lipid uptake mechanisms of lymphocyte suppression in malignant ascites. Therapeutically, these data point to LXRβ antagonism or restriction of local oxysterol biosynthesis as candidate strategies to restore $CD8^+$ T cell fitness in OC, complementing rather than substituting for checkpoint blockade, consistent with emerging interest in LXR-directed immunometabolic intervention in human disease[66].

MATERIALS AND METHODS

Patient samples. Ovarian carcinoma (OC) ascites was collected from untreated patients with high-grade serous ovarian carcinoma (HGSOC) prior to surgery at Marburg University Hospital. Cell-free ascites was cryopreserved at -80 °C (Table S1). The ethics committee at Philipps University approved the collection and analysis of human material (reference number 205/10). Donors provided written consent in accordance with the Declaration of Helsinki. Non-viral liver cirrhosis (LC) ascites was collected from patients with decompensated liver cirrhosis without spontaneous bacterial peritonitis, isolated during therapeutic large-volume paracentesis, at the Section of Translational Systems Immunology in Hepatogastroenterology, Department of Internal Medicine II (Gastroenterology, Hepatology, Endocrinology and Infectious Diseases), University Medical Center Freiburg. Samples were obtained from the HBUF/FREEZE biobank (IRB#474/14, Ethics Committee of the Albert-Ludwigs-University, Freiburg) and shipped to the study center for processing within 24 h. Cell-free ascites was cryopreserved at −80 °C.

Human $CD8^+$ T cell isolation and culture. Peripheral blood mononuclear cells (PBMCs) were isolated from leukoreduction system (LRS) chambers obtained from healthy donors (HD) provided by the Center for Transfusion Medicine and Hemotherapy at the University Hospital Gießen and Marburg (UKGM). PBMCs were isolated by density-gradient centrifugation using Lymphocyte Separation Medium (Capricorn Scientific). $CD8^+$ T cells were isolated from PBMCs using a negative selection: 3 x 10^7 PBMCs were incubated with FITC-conjugated antibodies against CD4 (clone RPA-T4, #300506, BioLegend), CD14 (clone M5E2, #325604, BioLegend), CD15 (clone W6D3, #301904, BioLegend), CD16 (clone 3G8, #302006, BioLegend), CD19 (clone HIB19, #302206, BioLegend), CD36 (clone 5-271, #336204, BioLegend) and CD56 (clone HCD56, #318304, BioLegend) for 30min at 4°C. Cells were washed and then incubated with anti-FITC-biotin/streptavidin complex (#Z7041, Promega) for 15 min, followed by two washes with MACS buffer PBS (#BSL1830-10, Biosell) containing 0.5% BSA (#A7906-100G, Sigma-Aldrich) and 2 mM EDTA (0.5 M, pH 8.0, #V4231, Promega). Labeled cells were incubated with biotin-coupled magnetic beads for 20 min on a rotator, then subjected to magnetic separation. Non-$CD8^+$ T cells were retained in the magnetic field. The flow-through fraction contained the $CD8^+$ T cells with approx. 95% purity. $CD8^+$ T cells were cultured in RPMI medium: RPMI 1640 supplemented with 2 mM glutamine, 1 % (v/v) nonessential amino acids, 1 % (v/v) sodium

pyruvate, penicillin (50 U ml^{-1}), streptomycin (50 mg ml^{-1}), and 10 % (v/v) Fetal calf serum (FCS). Reagents and antibodies are listed in Tables S2 and S3.

T cell activation. $CD8^+$ T cells were activated with human T cell activation and expansion (TAE) beads (CD3/CD28/CD2, #130-091-441, Miltenyi Biotec) at a 2:1 cell: bead ratio in RPMI or 100% acellular ascites (OC or LC), with or without the indicated treatments. Activation-marker and cytokine readouts were assessed after approximately 16 h of stimulation using antibodies against CD25 (BV421, #302629, BioLegend), CD69 (FITC, #310904, BioLegend), IFN-γ (APC, #502512, BioLegend; PE/Cy7, #502527, BioLegend), TNF (PE/Cy7, #502930, BioLegend; BV421, #502931, BioLegend), CD107a/LAMP-1 (PE, #328608, BioLegend) and IRF4 (AF647, #646408, BioLegend); proliferation was assessed after 5 days.

Flow cytometry. Surface staining was performed in PBS/2% FCS (30min). For intracellular cytokine staining, cells were restimulated with PMA (50 ng ml^{-1}) and ionomycin (1µg ml^{-1}, both from Sigma-Aldrich) in the presence of brefeldin A (5µg ml^{-1}; BioLegend) for 4 h, with CD107a added during restimulation. After restimulation, the cells were fixed with 2% paraformaldehyde, permeabilized, and stained with the respective antibodies. IRF4 staining was performed without restimulation using the FOXP3/Fixation-Kit (eBioscience, 00-5521-00). Viability was assessed with Zombie NIR Fixable Viability Kit (BioLegend, 423106), diluted 1:1000, with 10 µl added per 100 µl sample volume, and incubated for 5 minutes at room temperature. Samples were acquired on BD FACSymphony A1 and analyzed with FlowJo Software (FlowJo v10.10.0).

Proliferation assay. $CD8^+$ T cells were labeled with the proliferation dye eFluor 670 (2 µM; eBioscience™, 65-0840-85, used in Fig. 1I and Fig. 3C) for 10 minutes at 37 °C, protected from light. Cells were then washed, resuspended in culture medium, seeded in 96-well plates, and activated with TAE beads at a 2:1 cell: bead ratio. Proliferation was assessed by flow cytometry on day 5. For the proliferation experiment shown in Fig. 1E, isolated $CD8^+$ T cells were instead labeled with CFSE (CellTrace CFSE cell proliferation Kit; Thermo Fisher Scientific, #C34554). Per condition, 4×10^5 cells ml^{-1} were resuspended in 100 µl of CFSE master mix (5 µl CFSE in DMSO, diluted 1:1000 in PBS). Cells were incubated for 15 minutes at 37 °C in the dark, quenched with 500 µl PBS for 5 minutes at room temperature in the dark, then resuspended in pre-warmed RPMI, OC, or LC ascites. TAE beads were added at a 4:1 cell: bead ratio, using fewer beads than the standard protocol to limit T-cell exhaustion over the extended culture period

required for this assay. Cells were plated and incubated for 5 days at 37 °C, then washed twice, resuspended in 150 µl PBS, and analyzed by flow cytometry.

Phospho-flow cytometry (TCR proximal TCR signaling). For assessment of TCR-proximal signaling kinetics (Fig. 3F), $CD8^+$ T cells were activated on MaxiSorp plates (439454, Thermo Fisher) coated with anti-CD3 (clone TR66; Enzo Life Sciences, #ALX-804-822-C100) and anti -CD28 (BioLegend, #302914), each at 2 µg ml^{-1}, coated for 16 h at 4 °C, then rested in FCS-free medium at 37 °C for 4 h. Cells were then incubated with anti-CD3 (clone TR66; Enzo Life Sciences) for 10 min on ice and stained with a live/dead Zombie viability dye (BioLegend). Cells were washed and incubated with AffiniPure $F(ab')_2$ fragment goat anti-mouse IgG, Fcγ fragment specific (Jackson ImmunoResearch, #115-006-071), 13 µg ml^{-1}, to cross-link surface-bound anti-CD3 and trigger TCR signaling, for the indicated time points (0, 0.5, 1, 2 and 5 min). Immediately after cross-linking, cells were fixed in Lyse/Fix buffer (BD Biosciences) at 37 °C for 10 min, then permeabilized in pre-cooled BD Perm buffer (BD Biosciences) on ice for 30 min. Cells were then stained with antibodies against phospho-Lck (Tyr394; clone A18002D, BioLegend, #933104, PE), phospho-Zap70 (pY292; clone J34-602, BD Biosciences, #558510, PE), phospho-PLCγ1 (pY783, BD Biosciences, #557883, AF647) and phospho-ERK1/2 (pT202/pY204; clone 6B8B69, BioLegend, #369509, BV421) for 30 min at room temperature. Samples were acquired on a BD FACSymphony A1 and analyzed with FlowJo (FlowJo v10.10.0).

TCR surface expression time course. $CD8^+$ T cells were activated using the same plate-bound anti-CD3/anti-CD28 protocol as described above for phospho-flow cytometry (Fig. 3F). Cells were then washed to remove the activation stimulus before resting. Surface TCRα/β expression was assessed by flow cytometry using APC anti-human TCR α/β (BioLegend, #306718) before activation, after 16 h of activation, and after an additional 6 h or 24 h of resting.

siRNA-mediated IRF4 knockdown. An Amaxa Human T cell Nucleofector Kit (VPA 1002, Lonza) was used to knock down human IRF4 by siRNA in $CD8^+$ T cells according to the manufacturer's instructions. $CD8^+$ T cells ($5x10^6$) were nucleofected with 10 nM IRF4-specific siRNA (cat. 4392420, Thermofisher) or 10 nM control scrambled RNA (cat. 4390843, Thermofisher) by the T-23 transfection program (Amaxa). After 5 hours, the media was changed, and cells were activated with Dynabeads Human T-Activator CD3/CD28 (11131D, Thermo Fisher) overnight, followed by flow cytometric analysis.

RNA-Seq analysis and bioinformatics. $CD8^+$ T cells isolated from PB of HD (n=12) were stimulated with TAE beads in control media RPMI (n=12) or in ascites from 41 different patients (n=41) for 16 h. Then, live $CD8^+$ T cells were sorted using FACSAria™ III (BD Biosciences). RNA was purified with the RNeasy Plus Micro Kit (50) according to the manufacturer's protocol (Qiagen, #74034). RNA quality was assessed using the Experion RNA StdSens Analysis Kit (Bio-Rad). RNAseq libraries were prepared from total RNA using the QuantSeq 3' mRNA-Seq Library Prep Kit FWD for Illumina (Lexogen) in combination with the UMI Second Strand Synthesis Module for QuantSeq FWD (Illumina, Read 1) (Lexogen) according to the manufacturer's instructions. Quality of sequencing libraries was controlled on a Bioanalyzer 2100 using the Agilent High Sensitivity DNA Kit (Agilent). Pooled sequencing libraries were quantified and sequenced on the NextSeq550 platform (Illumina) with 75-base single reads.

Raw sequencing reads were aligned using STAR 2.6.1d[67] against the Ensembl[68] Homo sapiens genome revision 100 (assembly GRCh38). Unique-molecular-identifier deduplication was performed using umi-tools 1.1.0[69], and gene expression was quantified against Ensembl gene models for protein-coding genes using custom Python scripts. Genes were filtered to those with at least 30 'Counts per million' in at least one sample and a three-fold difference between the lowest and highest expression samples. Genes were tested for differential expression with limma / Deseq2 / (t-test & Benjamini Hochberg correction)[70,71], blocked on $CD8^+$ T cell donors, and filtered for a two-fold change and a False Discovery Rate of 0.1 with all three tests. All clustering and plotting were performed on TMM-normalized expression values (calculated via edgeR)[72], which were "batch corrected" for the $CD8^+$ T cell donors. We deposited raw sequencing data at Array Express (E-MTAB- 17736).

Quantitative PCR. Treated $CD8^+$ T cells were harvested, washed in PBS, and RNA was isolated using the EXTRACTME Total RNA Kit (Blirt, EM09.2-250). RNA concentration was measured by NanoDrop (Thermo Fisher), then stored at −80 °C. cDNA was synthesized with the RevertAid First Strand cDNA Synthesis Kit (Thermo Fisher Scientific, K1622) and stored at −20 °C. RT-qPCR was performed with SYBR Green (ABclonal, RK2103) to measure *HMGCR*, *MYLIP*, *ABCG1*, *SQLE*, *IRF4*, *ABCA1*, *LXRβ,* and *SREBF1* normalized to *18S* (primer sequences are listed in Table S5), and analyzed using the $2^{-}\Delta\Delta Ct$ method. Per reaction, 10 ng cDNA was added to a master mix of H_2O, SYBR Green, and forward/reverse primers (10 µM); cycling was 95 °C for 3 min,

then cycles of 95 °C for 10 s and 60 °C for 30 s, followed by a melt curve (65–95 °C, 0.5 °C/5 s steps).

Lipidomics. $CD8^+$ T cell pellets were prepared to minimize autoxidation and chemical contamination prior to shipment for lipidomics/epilipidomics analysis. Cells were washed in PBS containing 1 μg ml^{-1} butylated hydroxytoluene (BHT; Sigma-Aldrich, #W218405;) and collected on ice using pre-cooled, BHT-containing buffers throughout, with approximately 1–3 × 10^6 cells per replicate. Pellets were stored in 0.5 mL PBS/BHT in original 2 mL Eppendorf Safe-Lock tubes at −80 °C, avoiding freeze–thaw cycles, and shipped on dry ice. Lipid extraction and LC-MS-based lipidomic/epilipidomic analysis were performed externally by the group of Dr. Maria Fedorova (Center of Membrane Biochemistry and Lipid Research, Faculty of Medicine Carl Gustav Carus, TU Dresden). Before extraction, samples were thawed on ice, and isotopically labeled internal standards were added (2 µL SPLASH®LIPIDOMIX® (Avanti Polar Lipids, Inc., Alabaster, AL, USA) and 2 µL Cer/Sph Mixture I (Avanti Polar Lipids, Inc.)). For lipid extraction, add 375 µL methanol (ULC-MS grade, > 99.97%; Biosolve B.V.), vortex, then add 750 µL chloroform (EMSURE ACS, ISO, Reag. Ph Eur; Supelco). Samples were incubated at 4°C for 1 h with slow rotation (40rpm). 625 µL of water was added for phase separation, vortexed, incubated for 10 min, and centrifuged for 10 min at 10,000 × g at 4°C. The lower organic phase was collected, dried under vacuum (40 mbar, 1200rpm), and stored at -80°C until MS analysis. Lipid extracts were reconstituted in 50 µL 2-propanol (ULC/MS-CC/SFC grade, >99.95%; Biosolve B.V.). Lipids were separated by reverse-phase chromatography (Accucore C30 column; 150 mm x 2.1 mm 2.6 µM 150 Å, Thermo Fisher Scientific) using a Vanquish Horizon UHPLC system (Thermo Fisher Scientific, Germering, Germany) coupled on-line to an Orbitrap Exploris 240 mass spectrometer (Thermo Fisher Scientific, Bremen, Germany) equipped with a HESI source. Lipids were separated at a flow rate of 0.3 mL/min and a column temperature of 50°C by a gradient elution starting at 10% B, increasing in 20 min to 80% B, followed by an increase to 95% B within 4 min, and further 3 min until 100% B is reached and kept for 5 min, followed by a decrease to 10%B within 0.1 min and equilibration at 10%B for 7.9 min. Eluent A consisted of acetonitrile:water (50:50, v/v, both ULC/MS-CC/SFC grade, Biosolve B.V.) and Eluent B of 2-propanol:acetonitrile:water (85:10:5, v/v/v), both containing 5 mM ammonium formate (MS grade, Sigma Aldrich) and 0.1 % formic acid (ULC/MS-CC/SFC grade, Biosolve B.V.)[73].

Full MS scans were acquired in positive and negative ionization mode with the following settings: spray voltage 3500 V/– 2500 V, sheath gas – 40 arb units, aux gas – 10 arb units, sweep gas – 1 arb unit, ion transfer tube – 300°C, vaporizer temperature – 370°C, EASY-IC run-start, default charge state – 1, resolution at m/z 200 – 120.000, normalized AGC target – 100%, maximum injection time – 100 ms, RF lens – 35%. Data-dependent acquisition (DDA) scans were acquired based on a cycle time of 1.3 s, a resolution of 15.000 at m/z 200, isolation window – 1.2 m/z, normalized stepped collision energies – 17,27,37 %, AGC target – 100%, maximum injection time – 60 ms, dynamic exclusion for 6s after two-times fragmentation within 6s. Acquired raw files were processed in Lipostar2 (Version 2.1.5b1)[74]. Briefly, super sample filters retaining only lipids with isotopic patterns and MS/MS were applied, and remaining MS/MS spectra were searched against the LIPID MAPS structural database (LMSD, downloaded 21.10.2023; addition of lipid standards using LipoStar DB manager). For identification, lipids with 3 and 4 stars were automatically approved, and searched for matching adducts and in-source fragments. Adducts were clustered and only approved features remained. These proposed identifications were manually checked for fragment matches and peak integration. Kendrick mass defect plots were used to validate the obtained identifications after manual inspection to filter out further false positive identifications. The data are expressed as pmol/µg of protein or pmol/µl of fluid.

Heatmaps and PCA plots (Fig. 4A, D) were generated in MetaboAnalyst (v 6.0), and volcano plots (Fig. 4B, C) in RStudio (R v4.4.0). Table S6 lists the detected lipids in $CD8^+$ T cells cultured under the described conditions. The list of upregulated lipids in OC ascites compared to RPMI/10% FCS media is provided in Table S7.

Targeted 27-HC quantification. 27-HC was quantified in ascites samples (n = 5 per group) by targeted GC-MS/MS. Briefly, 1 mL of OC ascites or LC ascites was spiked with 5 µL internal standard (100 µM 19-hydroxycholesterol) and extracted with 2 mL ice-cold acetonitrile. After 5 min on ice, samples were centrifuged and the supernatant dried overnight at 4°C. The residue was resuspended in 1 mL hexane and purified by solid-phase extraction (Chromabond unmodified silica cartridges, 100 mg/1 mL; Macherey-Nagel) as previously described [75], with oxysterols eluted in 2 mL of 30% isopropanol in hexane. Dried eluates were derivatized with MSTFA (20 µL) and pyridine (20 µL) at 40°C for 2 h and analyzed on an Agilent 7890A gas chromatograph coupled to a 7000 triple quadrupole mass spectrometer (splitless injection, 1

µL; HP-5MS column, 30 m × 0.25 mm, 0.25 µm film; helium carrier gas, 1 mL/min; inlet 250°C; transfer line 320°C). The oven temperature was held at 200°C for 1 min, ramped to 250°C at 25°C min^{-1}, then to 290°C at 15°C min^{-1}, and finally to 320°C at 5°C min^{-1} with a 7 min hold (total run time 18.67 min). The mass spectrometer was operated in positive electron impact ionization mode (70 eV, 35 µA electron current; source 230°C, quadrupole 150°C) using multiple reaction monitoring for 27-HC (m/z 129→73, 10 eV) and 19-HC (m/z 353→145, 15 eV), as described[76]. Quantification used a 6-point calibration curve (2–200 pmol); data were analyzed with MassHunter Quantitative Analysis (B.09.00).

Filipin III staining and fluorescence microscopy. Free cholesterol accumulation was visualized by Filipin III staining (Fig. 5D). Cells were plated onto poly-L-lysine-coated round glass coverslips and fixed in 4% paraformaldehyde (PFA) for 30–60 min at room temperature (500 µl of 16% PFA in PBS added directly to 2 ml medium); methanol-, ethanol-, or ethanol/acetone-based fixation was avoided as incompatible with lipid staining. Cells were washed with PBS, quenched for 5 min at room temperature in 1× TBS (50 mM Tris, 150 mM NaCl, pH 7.5), and stained with Filipin III (Tocris, #6250; diluted to 0.1 mg ml^{-1} in 5% BSA/TBS) for 30 min–1 h in the dark. Cells were washed 3× in TBS, rinsed in H_2O, and mounted in Mowiol. Microscopy was performed on a Leica Thunder Live Cell Imager equipped with an HC PL APO 63x/1.20 W CORR objective, LED8 illumination, Quad LED filter sets, and a K8 camera. Signal intensities of individual cells were quantified in Fiji: single cells were selected by drawing a region of interest (ROI), and corrected total cell fluorescence (CTCF) was calculated as integrated density minus (area of the selected cell × mean fluorescence of a background region).

Nile Red staining and lipid droplet quantification. $CD8^+$ T cells (3×10^5 ml^{-1}) were stained with Nile Red (Santa Cruz, sc-203747, 10 µM, 10 min, room temperature, dark), fixed (2% PFA, after Nile Red staining), and mounted in Roti-Mount FluorCare DAPI (Roth, HP20.1). Cells were imaged in two Nile Red channels: 515 nm ex./580 nm em. (Neutral lipids/cholesteryl esters) and 554 nm ex./640 nm em. (phospholipids). Lipid droplets were segmented in Fiji from the co-localized signal between these two Nile Red channels; nuclei were segmented from the DAPI channel (Otsu threshold, watershed), and cell bodies were approximated by 18-px Voronoi-constrained radial expansion.

Membrane order assay (Pro12A / generalized polarization). Plasma membrane order was assessed using the polarity-sensitive probe Pro12A kindly provided by Dr. Erdinç Sezgin, which

shifts its emission wavelength between an ordered (λ_Lo, 423 nm) and disordered (λ_Ld, 494 nm) state depending on local membrane packing (Fig. 5A). Cells were stained with Pro12A (final concentration 250 nM) for 1 min in flow cytometry tubes immediately prior to acquisition on a Cytek Aurora spectral flow cytometer (5 lasers, 64 channels). Generalized polarization (GP) was calculated as GP = (I_λLo − I_λLd) / (I_λLo + I_λLd).

27-Hydroxycholesterol treatment. $CD8^+$ T cells were activated overnight with TAE-beads (ratio 1:2) in RPMI supplemented with 27-hydroxycholesterol (Sigma-Aldrich, SML2042) (27-HC; 10 µM) or ethanol vehicle control (Fig. 6C, D; Supplementary Fig. 6B–D).

LXRβ pharmacology. LXRβ was inhibited with SR9243 (Cayman Chemical, Cay18420-5) (50 µM; pre-treatment for 3 h, 50% OC ascites, cells were activated overnight with TAE-beads; Fig. 6E–G, Supplementary Fig. 6G) or activated with GW3965 (Sigma-Aldrich, 405911-17-3) (2 µM; RPMI, no pre-treatment, cells were activated overnight with TAE-beads (ratio 1:2); Supplementary Fig. 6E, F), each with vehicle control, before assessment of CD25/CD69 and LXR/SREBP target gene expression (*ABCG1*, *MYLIP*, *SREBF1,* primers are listed in Table S5) by qPCR.

Quantification and statistical analysis. Statistical analyses were performed using GraphPad Prism (v10). Data are presented as bar graphs (mean ± SEM) unless otherwise indicated; in Fig. 5B, data are shown as violin plots with median and interquartile range. Each data point represents one biological replicate (an individual healthy donor or ascites sample), except in Fig. S4C, where representative data from n = 2 donors are shown and were not powered for statistical testing. We evaluated normality using the Shapiro-Wilk test. For two-group comparisons, we used two-tailed paired or unpaired Student's t-tests for normally distributed data; for comparisons across three or more matched conditions within the same donors, we used repeated-measures one-way ANOVA. We used the nonparametric Friedman test when repeated-measures data did not meet normality assumptions. One-way ANOVA without repeated-measures structure was used in Fig. S1A. Two-way ANOVA was used for time-course comparisons (Fig. 3F, G). We assessed the association between ascites and plasma cholesterol concentration (Fig. S2E) using Spearman correlation. A P value < 0.05 was considered statistically significant, indicated in figures as *P < 0.05, **P < 0.01, ***P < 0.001, ****P < 0.0001; ns = not significant.

REFERENCES

1. McMullen, M., Karakasis, K., Rottapel, R. & Oza, A. M. Advances in ovarian cancer, from biology to treatment. *Nature cancer* **2,** 6–8; 10.1038/s43018-020-00166-5 (2021).

2. Lisio, M.-A., Fu, L., Goyeneche, A., Gao, Z.-H. & Telleria, C. High-Grade Serous Ovarian Cancer: Basic Sciences, Clinical and Therapeutic Standpoints. *International journal of molecular sciences* **20,** 952; 10.3390/ijms20040952 (2019).

3. Ford, C. E., Werner, B., Hacker, N. F. & Warton, K. The untapped potential of ascites in ovarian cancer research and treatment. *British journal of cancer* **123,** 9–16; 10.1038/s41416-020-0875-x (2020).

4. Finkernagel, F. *et al.* Dual-platform affinity proteomics identifies links between the recurrence of ovarian carcinoma and proteins released into the tumor microenvironment. *Theranostics* **9,** 6601–6617; 10.7150/thno.37549 (2019).

5. Kipps, E., Tan, D. S. P. & Kaye, S. B. Meeting the challenge of ascites in ovarian cancer: new avenues for therapy and research. *Nature reviews. Cancer* **13,** 273–282; 10.1038/nrc3432 (2013).

6. Dietze, R. *et al.* Phosphoproteomics identify arachidonic-acid-regulated signal transduction pathways modulating macrophage functions with implications for ovarian cancer. *Theranostics* **11,** 1377–1395; 10.7150/thno.52442 (2021).

7. Hammoud, M. K. *et al.* Arachidonic acid, a clinically adverse mediator in the ovarian cancer microenvironment, impairs JAK-STAT signaling in macrophages by perturbing lipid raft structures. *Molecular oncology* **16,** 3146–3166; 10.1002/1878-0261.13221 (2022).

8. Reinartz, S. *et al.* Cell type-selective pathways and clinical associations of lysophosphatidic acid biosynthesis and signaling in the ovarian cancer microenvironment. *Molecular oncology* **13,** 185–201; 10.1002/1878-0261.12396 (2019).

9. Rana, S. V., Babu, S. G. V. & Kocchar, R. Usefulness of ascitic fluid cholesterol as a marker for malignant ascites. *Medical science monitor : international medical journal of experimental and clinical research* **11,** CR136-42 (2005).

10. Penet, M.-F. *et al.* Ascites Volumes and the Ovarian Cancer Microenvironment. *Frontiers in oncology* **8,** 595; 10.3389/fonc.2018.00595 (2018).

11. Anderson, A. S. *et al.* Metabolic changes during ovarian cancer progression as targets for sphingosine treatment. *Experimental cell research* **319,** 1431–1442; 10.1016/j.yexcr.2013.02.017 (2013).

12. Galon, J. & Bruni, D. Tumor Immunology and Tumor Evolution: Intertwined Histories. *Immunity* **52,** 55–81; 10.1016/j.immuni.2019.12.018 (2020).

13. Rausch, L. & Kallies, A. Molecular Mechanisms Governing CD8 T Cell Differentiation and Checkpoint Inhibitor Response in Cancer. *Annual review of immunology* **43,** 515–543; 10.1146/annurev-immunol-082223-044122 (2025).

14. van der Leun, A. M., Thommen, D. S. & Schumacher, T. N. CD8+ T cell states in human cancer: insights from single-cell analysis. *Nature reviews. Cancer* **20,** 218–232; 10.1038/s41568-019-0235-4 (2020).

15. McLane, L. M., Abdel-Hakeem, M. S. & Wherry, E. J. CD8 T Cell Exhaustion During Chronic Viral Infection and Cancer. *Annual review of immunology* **37,** 457–495; 10.1146/annurev-immunol-041015-055318 (2019).

16. Miller, B. C. *et al.* Subsets of exhausted CD8+ T cells differentially mediate tumor control and respond to checkpoint blockade. *Nature immunology* **20,** 326–336; 10.1038/s41590-019-0312-6 (2019).

17. Worzfeld, T. *et al.* The Unique Molecular and Cellular Microenvironment of Ovarian Cancer. *Frontiers in oncology* **7,** 24; 10.3389/fonc.2017.00024 (2017).

18. Sato, E. *et al.* Intraepithelial CD8+ tumor-infiltrating lymphocytes and a high CD8+/regulatory T cell ratio are associated with favorable prognosis in ovarian cancer. *Proceedings of the National Academy of Sciences of the United States of America* **102,** 18538–18543; 10.1073/pnas.0509182102 (2005).

19. Zhang, L. *et al.* Intratumoral T cells, recurrence, and survival in epithelial ovarian cancer. *The New England journal of medicine* **348,** 203–213; 10.1056/NEJMoa020177 (2003).

20. Robert, C. A decade of immune-checkpoint inhibitors in cancer therapy. *Nature communications* **11,** 3801; 10.1038/s41467-020-17670-y (2020).

21. Färkkilä, A. *et al.* Immunogenomic profiling determines responses to combined PARP and PD-1 inhibition in ovarian cancer. *Nature communications* **11,** 1459; 10.1038/s41467-020-15315-8 (2020).

22. Borella, F. *et al.* Immune Checkpoint Inhibitors in Epithelial Ovarian Cancer: An Overview on Efficacy and Future Perspectives. *Diagnostics (Basel, Switzerland)* **10**; 10.3390/diagnostics10030146 (2020).

23. Lieber, S. *et al.* Prognosis of ovarian cancer is associated with effector memory CD8+ T cell accumulation in ascites, CXCL9 levels and activation-triggered signal transduction in T cells. *Oncoimmunology* **7,** e1424672; 10.1080/2162402X.2018.1424672 (2018).

24. Simpson-Abelson, M. R. *et al.* Human ovarian tumor ascites fluids rapidly and reversibly inhibit T cell receptor-induced NF-κB and NFAT signaling in tumor-associated T cells. *Cancer immunity* **13,** 14 (2013).

25. Song, M. *et al.* IRE1α-XBP1 controls T cell function in ovarian cancer by regulating mitochondrial activity. *Nature* **562,** 423–428; 10.1038/s41586-018-0597-x (2018).

26. Bietz, A., Zhu, H., Xue, M. & Xu, C. Cholesterol Metabolism in T Cells. *Frontiers in immunology* **8,** 1664; 10.3389/fimmu.2017.01664 (2017).

27. Chen, Y. *et al.* Cholesterol inhibits TCR signaling by directly restricting TCR-CD3 core tunnel motility. *Molecular cell* **82,** 1278-1287.e5; 10.1016/j.molcel.2022.02.017 (2022).

28. Gao, Y. *et al.* T cell cholesterol transport links intestinal immune responses to dietary lipid absorption. *American Association for the Advancement of Science* (2025).

29. Harberts, A. *et al.* Interferon regulatory factor 4 controls effector functions of CD8+ memory T cells. *Proceedings of the National Academy of Sciences of the United States of America* **118,** e2014553118; 10.1073/pnas.2014553118 (2021).

30. Raczkowski, F. *et al.* The transcription factor Interferon Regulatory Factor 4 is required for the generation of protective effector CD8+ T cells. *Proceedings of the National Academy of Sciences of the United States of America* **110,** 15019–15024; 10.1073/pnas.1309378110 (2013).

31. Man, K. *et al.* Erratum: Corrigendum: The transcription factor IRF4 is essential for TCR affinity–mediated metabolic programming and clonal expansion of T cells. *Nat Immunol* **15,** 894; 10.1038/ni0914-894b (2014).

32. Luo, J., Yang, H. & Song, B.-L. Mechanisms and regulation of cholesterol homeostasis. *Nature reviews. Molecular cell biology* **21,** 225–245; 10.1038/s41580-019-0190-7 (2020).

33. Shimano, H. & Sato, R. SREBP-regulated lipid metabolism: convergent physiology - divergent pathophysiology. *Nature reviews. Endocrinology* **13,** 710–730; 10.1038/nrendo.2017.91 (2017).

34. Michaels, A. J., Campbell, C., Bou-Puerto, R. & Rudensky, A. Y. Nuclear receptor LXRβ controls fitness and functionality of activated T cells. *The Journal of experimental medicine* **218**; 10.1084/jem.20201311 (2021).

35. Yan, C. *et al.* Exhaustion-associated cholesterol deficiency dampens the cytotoxic arm of antitumor immunity. *Cancer cell* **41,** 1276-1293.e11; 10.1016/j.ccell.2023.04.016 (2023).

36. Baek, A. E. *et al.* The cholesterol metabolite 27 hydroxycholesterol facilitates breast cancer metastasis through its actions on immune cells. *Nature communications* **8,** 864; 10.1038/s41467-017-00910-z (2017).

37. Gaud, G., Lesourne, R. & Love, P. E. Regulatory mechanisms in T cell receptor signalling. *Nature reviews. Immunology* **18,** 485–497; 10.1038/s41577-018-0020-8 (2018).

38. Bhattacharyya, N. D. & Feng, C. G. Regulation of T Helper Cell Fate by TCR Signal Strength. *Frontiers in immunology* **11,** 624; 10.3389/fimmu.2020.00624 (2020).

39. Kidani, Y. *et al.* Sterol regulatory element-binding proteins are essential for the metabolic programming of effector T cells and adaptive immunity. *Nature immunology* **14,** 489–499; 10.1038/ni.2570 (2013).

40. Wu, Z. *et al.* Interleukin-21 receptor gene induction in human T cells is mediated by T-cell receptor-induced Sp1 activity. *Molecular and cellular biology* **25,** 9741–9752; 10.1128/MCB.25.22.9741-9752.2005 (2005).

41. Conley, J. M., Gallagher, M. P., Rao, A. & Berg, L. J. Activation of the Tec Kinase ITK Controls Graded IRF4 Expression in Response to Variations in TCR Signal Strength. *Journal*

of immunology (Baltimore, Md. : 1950) **205,** 335–345; 10.4049/jimmunol.1900853 (2020).

42. Redmond, W. L., Ruby, C. E. & Weinberg, A. D. The role of OX40-mediated co-stimulation in T-cell activation and survival. *Critical reviews in immunology* **29,** 187–201; 10.1615/critrevimmunol.v29.i3.10 (2009).

43. Hornburg, M. *et al.* Single-cell dissection of cellular components and interactions shaping the tumor immune phenotypes in ovarian cancer. *Cancer cell* **39,** 928-944.e6; 10.1016/j.ccell.2021.04.004 (2021).

44. Wang, B. & Tontonoz, P. Liver X receptors in lipid signalling and membrane homeostasis. *Nature reviews. Endocrinology* **14,** 452–463; 10.1038/s41574-018-0037-x (2018).

45. Reinartz, S. *et al.* A transcriptome-based global map of signaling pathways in the ovarian cancer microenvironment associated with clinical outcome. *Genome biology* **17,** 108; 10.1186/s13059-016-0956-6 (2016).

46. Tall, A. R. & Yvan-Charvet, L. Cholesterol, inflammation and innate immunity. *Nature reviews. Immunology* **15,** 104–116; 10.1038/nri3793 (2015).

47. Westerterp, M. *et al.* Cholesterol Efflux Pathways Suppress Inflammasome Activation, NETosis, and Atherogenesis. *Circulation* **138,** 898–912; 10.1161/CIRCULATIONAHA.117.032636 (2018).

48. Courtney, A. H., Lo, W.-L. & Weiss, A. TCR Signaling: Mechanisms of Initiation and Propagation. *Trends in biochemical sciences* **43,** 108–123; 10.1016/j.tibs.2017.11.008 (2018).

49. Evnouchidou, I., Caillens, V., Koumantou, D. & Saveanu, L. The role of endocytic trafficking in antigen T cell receptor activation. *Biomedical journal* **45,** 310–320; 10.1016/j.bj.2021.09.004 (2022).

50. van Dierendonck, X. A. M. H. *et al.* Triglyceride breakdown from lipid droplets regulates the inflammatory response in macrophages. *Proceedings of the National Academy of Sciences of the United States of America* **119,** e2114739119; 10.1073/pnas.2114739119 (2022).

51. Lim, S. A., Su, W., Chapman, N. M. & Chi, H. Lipid metabolism in T cell signaling and function. *Nature chemical biology* **18,** 470–481; 10.1038/s41589-022-01017-3 (2022).

52. Wu, W., Shi, X. & Xu, C. Regulation of T cell signalling by membrane lipids. *Nature reviews. Immunology* **16,** 690–701; 10.1038/nri.2016.103 (2016).

53. Amaro, M., Reina, F., Hof, M., Eggeling, C. & Sezgin, E. Laurdan and Di-4-ANEPPDHQ probe different properties of the membrane. *Journal of physics D: Applied physics* **50,** 134004; 10.1088/1361-6463/aa5dbc (2017).

54. Ragaller, F. *et al.* Quantifying Fluorescence Lifetime Responsiveness of Environment-Sensitive Probes for Membrane Fluidity Measurements. *The journal of physical chemistry. B* **128,** 2154–2167; 10.1021/acs.jpcb.3c07006 (2024).

55. Harder, T., Rentero, C., Zech, T. & Gaus, K. Plasma membrane segregation during T cell activation: probing the order of domains. *Current opinion in immunology* **19,** 470–475; 10.1016/j.coi.2007.05.002 (2007).

56. Umetani, M. *et al.* 27-Hydroxycholesterol is an endogenous SERM that inhibits the cardiovascular effects of estrogen. *Nature medicine* **13,** 1185–1192; 10.1038/nm1641 (2007).

57. Radhakrishnan, A., Ikeda, Y., Kwon, H. J., Brown, M. S. & Goldstein, J. L. Sterol-regulated transport of SREBPs from endoplasmic reticulum to Golgi: oxysterols block transport by binding to Insig. *Proceedings of the National Academy of Sciences of the United States of America* **104,** 6511–6518; 10.1073/pnas.0700899104 (2007).

58. Bensinger, S. J. & Tontonoz, P. Integration of metabolism and inflammation by lipid-activated nuclear receptors. *Nature* **454,** 470–477; 10.1038/nature07202 (2008).

59. Fernandes, R. A. *et al.* A cell topography-based mechanism for ligand discrimination by the T cell receptor. *Proceedings of the National Academy of Sciences of the United States of America* **116,** 14002–14010; 10.1073/pnas.1817255116 (2019).

60. Ma, X. *et al.* Cholesterol Induces CD8+ T Cell Exhaustion in the Tumor Microenvironment. *Cell metabolism* **30,** 143-156.e5; 10.1016/j.cmet.2019.04.002 (2019).

61. Slattery, K. *et al.* Uptake of lipids from ascites drives NK cell metabolic dysfunction in ovarian cancer. *American Association for the Advancement of Science* (2025).

62. Ecker, C. *et al.* Differential Reliance on Lipid Metabolism as a Salvage Pathway Underlies Functional Differences of T Cell Subsets in Poor Nutrient Environments. *Cell reports* **23,** 741–755; 10.1016/j.celrep.2018.03.084 (2018).

63. Geltink, R. I. K., Kyle, R. L. & Pearce, E. L. Unraveling the Complex Interplay Between T Cell Metabolism and Function. *Annual review of immunology* **36,** 461–488; 10.1146/annurev-immunol-042617-053019 (2018).

64. Dang, E. V., McDonald, J. G., Russell, D. W. & Cyster, J. G. Oxysterol Restraint of Cholesterol Synthesis Prevents AIM2 Inflammasome Activation. *Cell* **171,** 1057-1071.e11; 10.1016/j.cell.2017.09.029 (2017).

65. Brown, E. G. *et al.* Lipids in ovarian cancer ascites impair T cell activation by disrupting TCR dynamics. *Nature metabolism* **8,** 1508–1527; 10.1038/s42255-026-01557-1 (2026).

66. Tavazoie, M. F. *et al.* LXR/ApoE Activation Restricts Innate Immune Suppression in Cancer. *Cell* **172,** 825-840.e18; 10.1016/j.cell.2017.12.026 (2018).

67. Dobin, A. *et al.* STAR: ultrafast universal RNA-seq aligner. *Bioinformatics (Oxford, England)* **29,** 15–21; 10.1093/bioinformatics/bts635 (2013).

68. Cunningham, F. *et al.* Ensembl 2022. *Nucleic acids research* **50,** D988-D995; 10.1093/nar/gkab1049 (2022).

69. Smith, T., Heger, A. & Sudbery, I. UMI-tools: modeling sequencing errors in Unique Molecular Identifiers to improve quantification accuracy. *Genome research* **27,** 491–499; 10.1101/gr.209601.116 (2017).

70. Love, M. I., Huber, W. & Anders, S. Moderated estimation of fold change and dispersion for RNA-seq data with DESeq2. *Genome biology* **15,** 550; 10.1186/s13059-014-0550-8 (2014).

71. Ritchie, M. E. *et al.* limma powers differential expression analyses for RNA-sequencing and microarray studies. *Nucleic acids research* **43,** e47; 10.1093/nar/gkv007 (2015).

72. Robinson, M. D., McCarthy, D. J. & Smyth, G. K. edgeR: a Bioconductor package for differential expression analysis of digital gene expression data. *Bioinformatics (Oxford, England)* **26,** 139–140; 10.1093/bioinformatics/btp616 (2010).

73. Wölk, M. & Fedorova, M. Recommendations for Accurate Lipid Annotation and Semi-absolute Quantification from LC-MS/MS Datasets. *Methods in molecular biology (Clifton, N.J.)* **2855,** 269–287; 10.1007/978-1-0716-4116-3_16 (2025).

74. Goracci, L. *et al.* Lipostar, a Comprehensive Platform-Neutral Cheminformatics Tool for Lipidomics. *Analytical chemistry* **89,** 6257–6264; 10.1021/acs.analchem.7b01259 (2017).

75. Koch, E. *et al.* GC-MS analysis of oxysterols and their formation in cultivated liver cells (HepG2). *Lipids* **58,** 41–56; 10.1002/lipd.12360 (2023).

76. Saito, H., Nishimura, M., Sato, R. & Yamauchi, Y. Quantitative Determination of Cholesterol Hydroxylase Specificities by GC-MS/MS in Living Mammalian Cells. *Bio-protocol* **14,** e4924; 10.21769/BioProtoc.4924 (2024).

ACKNOWLEDGEMENTS

We thank Dr. Maria Fedorova for performing lipidomics; Dr. Yajuan Zhang for the initial steps in this project before the first author took over and for her foundational contributions; Achim Allmeroth and Traute Plaum for preparing and processing the ovarian cancer ascites samples; and Dr. Luca Simeoni and Dr. Ondrej Stepanek for providing reagents and helpful advice.

AUTHOR CONTRIBUTIONS

MH and AJ conceived and designed the study. AJ, SL, VL, HR, LK, CG and JP performed experiments. AJ, FF, AN, CG and JP analyzed the data. AN and TS performed sequencing. UW and SR provided OC samples. KR provided microscopy support. UC and MG performed lipidomics analysis. VT and JP performed metabolomics analysis. AJ and MH drafted the original manuscript. AJ, MH, and AB edited the manuscript.

FUNDING

This work was supported by the German Research Foundation (DFG; reference number 662844, project number HU 1824/9-1 to M.H.) and by the DFG-funded Research Training Group GRK2573 (second cohort; project number 416910386).

Competing interests

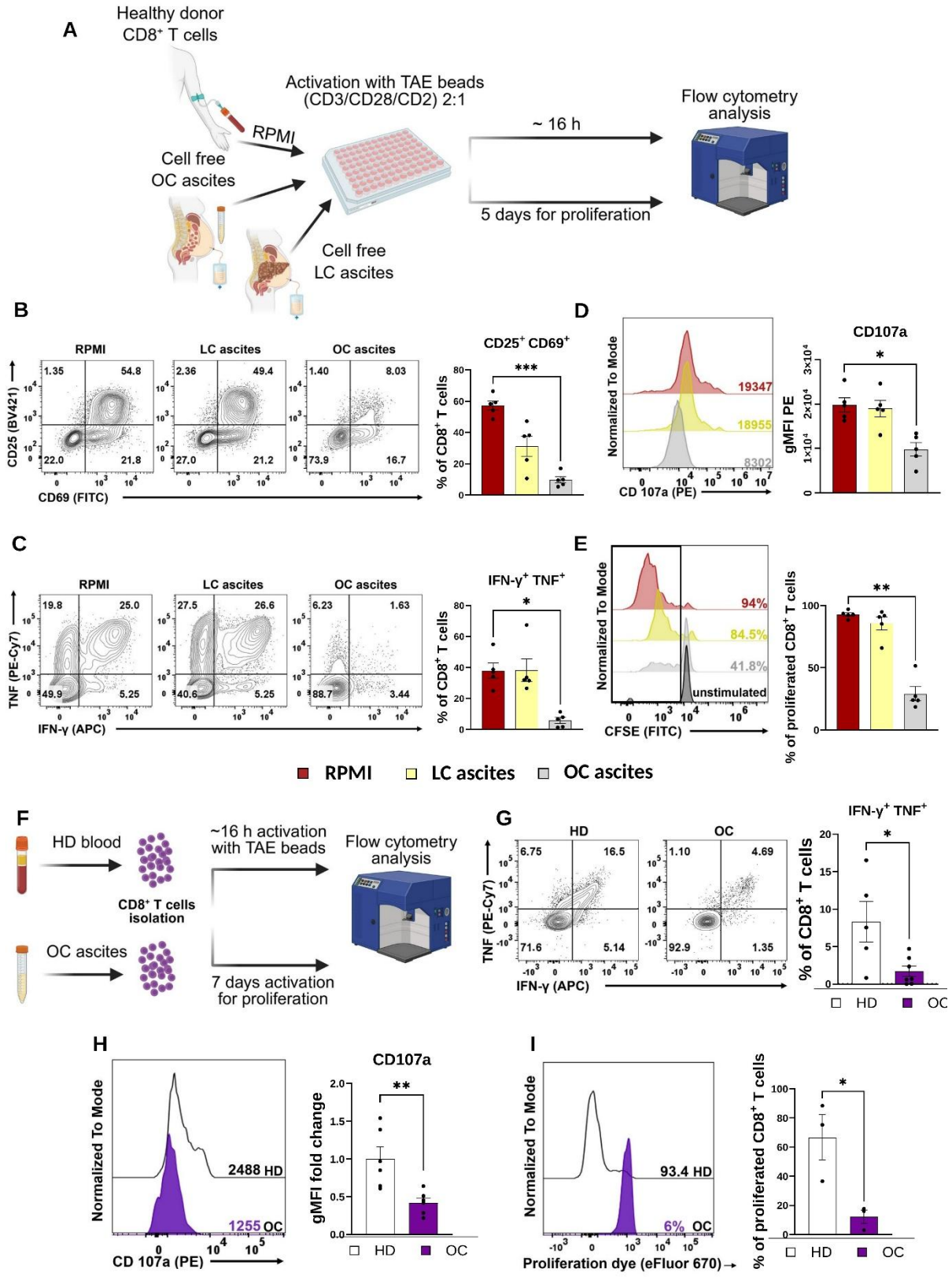
The authors declare no competing interests.

DATA AVAILABILITY STATEMENT

Bulk-seq data have been deposited at ArrayExpress under the accession code E-MTAB-17736. All other data are available in the article, source data and Supplementary Information, or from the corresponding author upon request. Source data are provided with this paper. Supplementary information is available at Cellular & Molecular Immunology´s website.

953 **FIGURE**

Figure 1



954

Figure 1. OC ascites suppresses TCR-driven activation and function of $CD8^+$ T cells. (A) Schematic of the experimental design. $CD8^+$ T cells isolated from HD PBMCs were cultured in RPMI, cell-free LC ascites, or cell-free OC ascites and stimulated for 16 h with TAE beads (anti-CD3/CD28/CD2, cell: beads ratio 2:1) Created in BioRender. Jouria, A. (2027) https://BioRender.com/fdi837b. (B-E) Flow cytometric analysis of HD $CD8^+$ T cells activated under conditions described in (A). (B) Frequency of $CD25^+CD69^+$ double-positive cells. (C) Frequency of $IFN\gamma^+TNF^+$ double-positive cells. (D) Degranulation assessed by CD107a surface expression (gMFI fold change). (E) Proliferation assessed by CFSE dilution. Data represent mean ± SEM from n = 5 independent donors. Statistical analysis: repeated-measures one-way ANOVA with Tukey's post hoc correction (B, D); Friedman test (C, E). $*P < 0.05$, $**P < 0.01$, $***P < 0.001$, $****P < 0.0001$. (F) Schematic of the experimental design for panels (G–I). $CD8^+$ T cells were isolated directly from HD peripheral blood (HD) or from OC ascites (OC) and stimulated for 16 h with TAE beads (2:1) Created in BioRender. Jouria, A. (2026) https://BioRender.com/j7wzkxc. (G–I) Functional analysis of HD blood-derived and OC ascites-resident $CD8^+$ T cells following stimulation as in (F). (G) Frequency of $IFN\gamma^+TNF^+$ double-positive cells (HD n = 5, OC n = 7). (H) CD107a gMFI fold change relative to controls (n = 6). (I) Proliferation assessed by eFluor670 dilution (n = 3). Statistical analysis: unpaired two-tailed *t*-test. $*P < 0.05$, $**P < 0.01$.

Figure 2

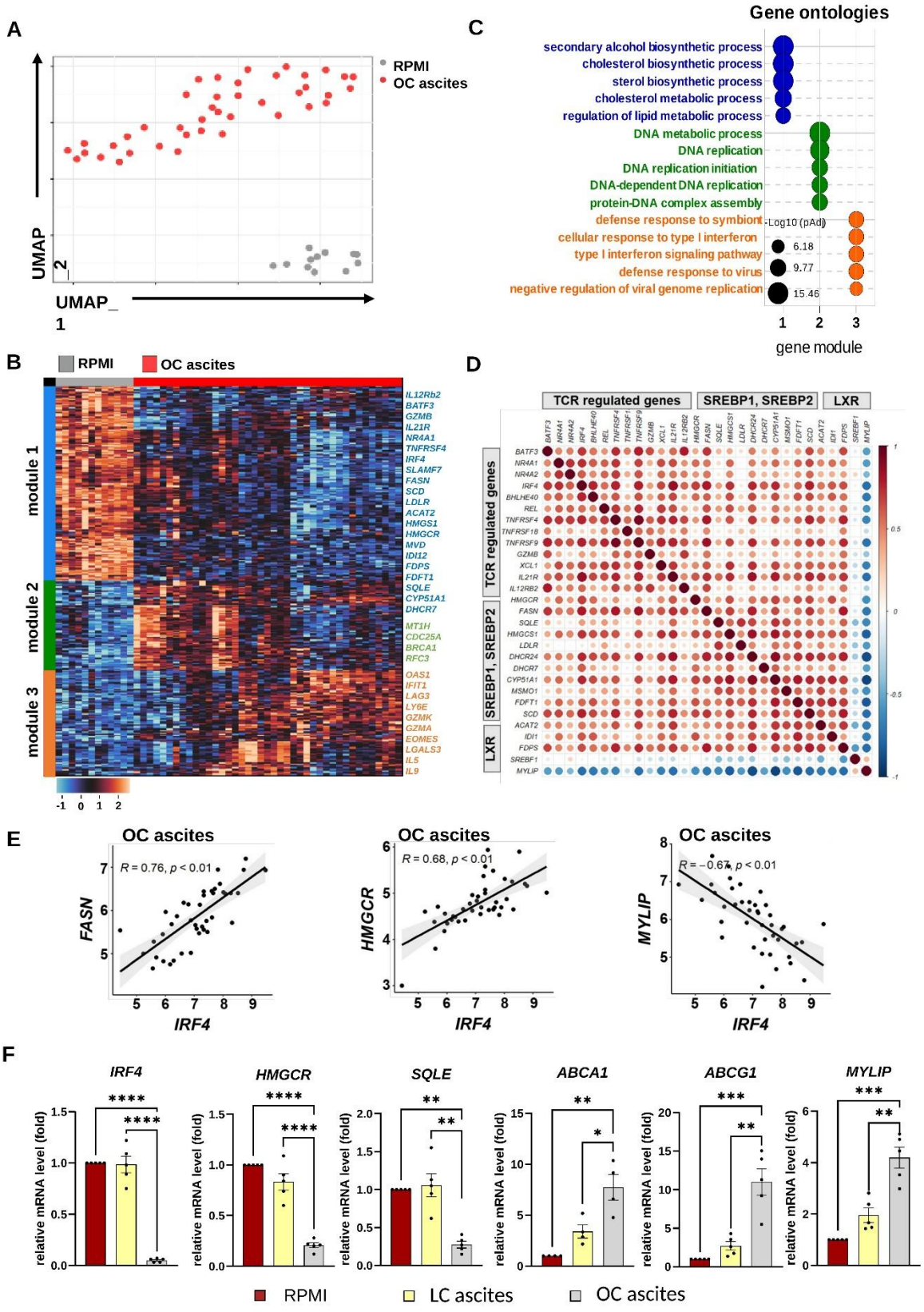
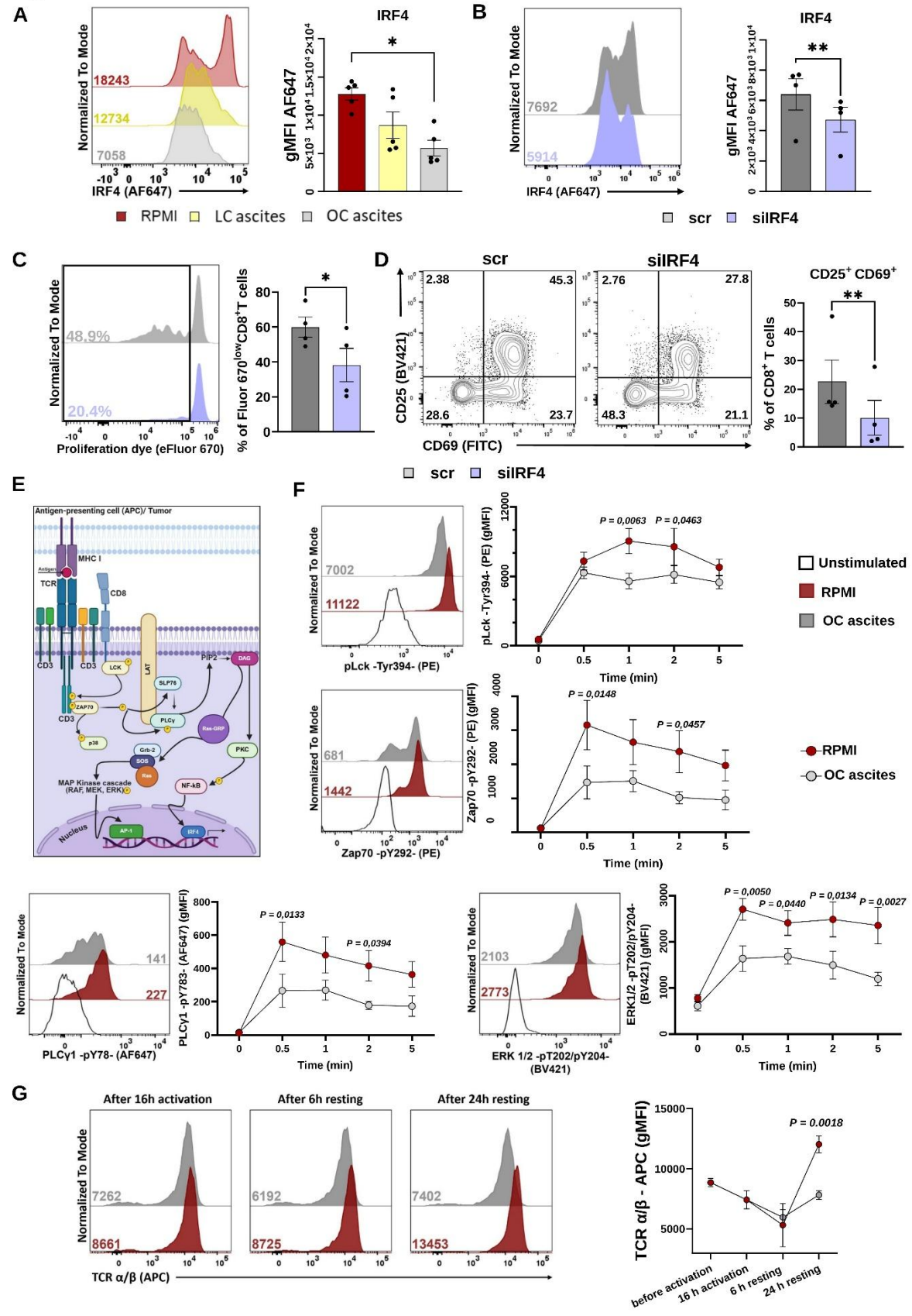

A
RPMI
OC ascites
UMAP_2
UMAP_1
C
Gene ontologies
secondary alcohol biosynthetic process
cholesterol biosynthetic process
sterol biosynthetic process
cholesterol metabolic process
regulation of lipid metabolic process
DNA metabolic process
DNA replication
DNA replication initiation
DNA-dependent DNA replication
protein-DNA complex assembly
defense response to symbiont
cellular response to type I interferon
type I interferon signaling pathway
defense response to virus
negative regulation of viral genome replication
-Log10 (pAdj)
6.18
9.77
15.46
1 2 3
gene module
B
RPMI
OC ascites
module 1
module 2
module 3
IL12Rb2
BATF3
GZMB
IL21R
NR4A1
TNFRSF4
IRF4
SLAMF7
FASN
SCD
LDLR
ACAT2
HMGS1
HMGCR
MVD
IDI12
FDPS
FDFT1
SQLE
CYP51A1
DHCR7
MT1H
CDC25A
BRCA1
RFC3
OAS1
IFIT1
LAG3
LY6E
GZMK
GZMA
EOMES
LGALS3
IL5
IL9
-1 0 1 2
D
TCR regulated genes
SREBP1, SREBP2
LXR
E
OC ascites
R = 0.76, p < 0.01
FASN
IRF4
OC ascites
R = 0.68, p < 0.01
HMGCR
IRF4
OC ascites
R = −0.67, p < 0.01
MYLIP
IRF4
F
IRF4
HMGCR
SQLE
ABCA1
ABCG1
MYLIP
relative mRNA level (fold)
RPMI
LC ascites
OC ascites

Figure 2. OC ascites reprograms the SREBP pathway and co-regulates LXRβ and TCR signaling gene expression in CD8⁺ T cells. (A-E) CD8⁺ T cells isolated from 12 HD PBMCs were activated with TAE beads (2:1) for 16 h in the presence of individual OC ascites samples (n = 41 independent patient samples) or RPMI (n = 12, used as a control for OC ascites). Viable CD8⁺ T cells were FACS-sorted after activation and subjected to bulk RNA-seq (QuantSeq 3' mRNA-Seq platform). (A) UMAP plot of RNA-seq analysis of CD8⁺ T cells activated in the presence of OC ascites (red, n=41) or in RPMI (grey, n=12). (B) Heatmap of differentially expressed genes (Z-score normalized, logFC ≥ 1; FDR ≤ 0.1) in CD8⁺ T cells after activation in the presence of OC ascites (n=41) or RPMI (n=12) for 16 h, classified into three modules based on mutual up- or down-regulation. (C) Gene Ontology (GO) biological process enrichment analysis. Bubble plots display the five most significantly enriched GO terms (ranked by $-\log_{10}$(padj)) for each of the three transcriptional modules defined in (B). The bubble area is proportional to the number of genes contributing to each term. (D) Distance correlation matrix displaying the dependence between lipid metabolism transcripts (SREBP1/2 and LXR target genes) and TCR signaling-associated genes, based on RNA-Seq from A, B. A distance correlation of zero indicates statistical independence between two transcripts, while values closer to 1 indicate stronger dependence. (E) Pearson correlation of *FASN*, *HMGCR*, *MYLIP*, and *IRF4* expression based on RNA-Seq from A and B, values are shown as log2 counts per million (CPM) after TMM normalization. (F) RT-qPCR validation of selected transcripts in CD8⁺ T cells activated as in Fig. 1 in RPMI, LC ascites, or OC ascites (n = 5 HD). Expression was normalized to 18S rRNA and the RPMI condition. *HMGCR* and *SQLE* are SREBP1/2 target genes; *ABCA1*, *ABCG1*, and *MYLIP* are LXR target genes; *IRF4* is a TCR activation–responsive transcription factor. Data represent mean ± SEM. Repeated-measures one-way ANOVA. **P* < 0.05, ***P* < 0.01, ****P* < 0.001, *****P* < 0.0001.

Figure 3

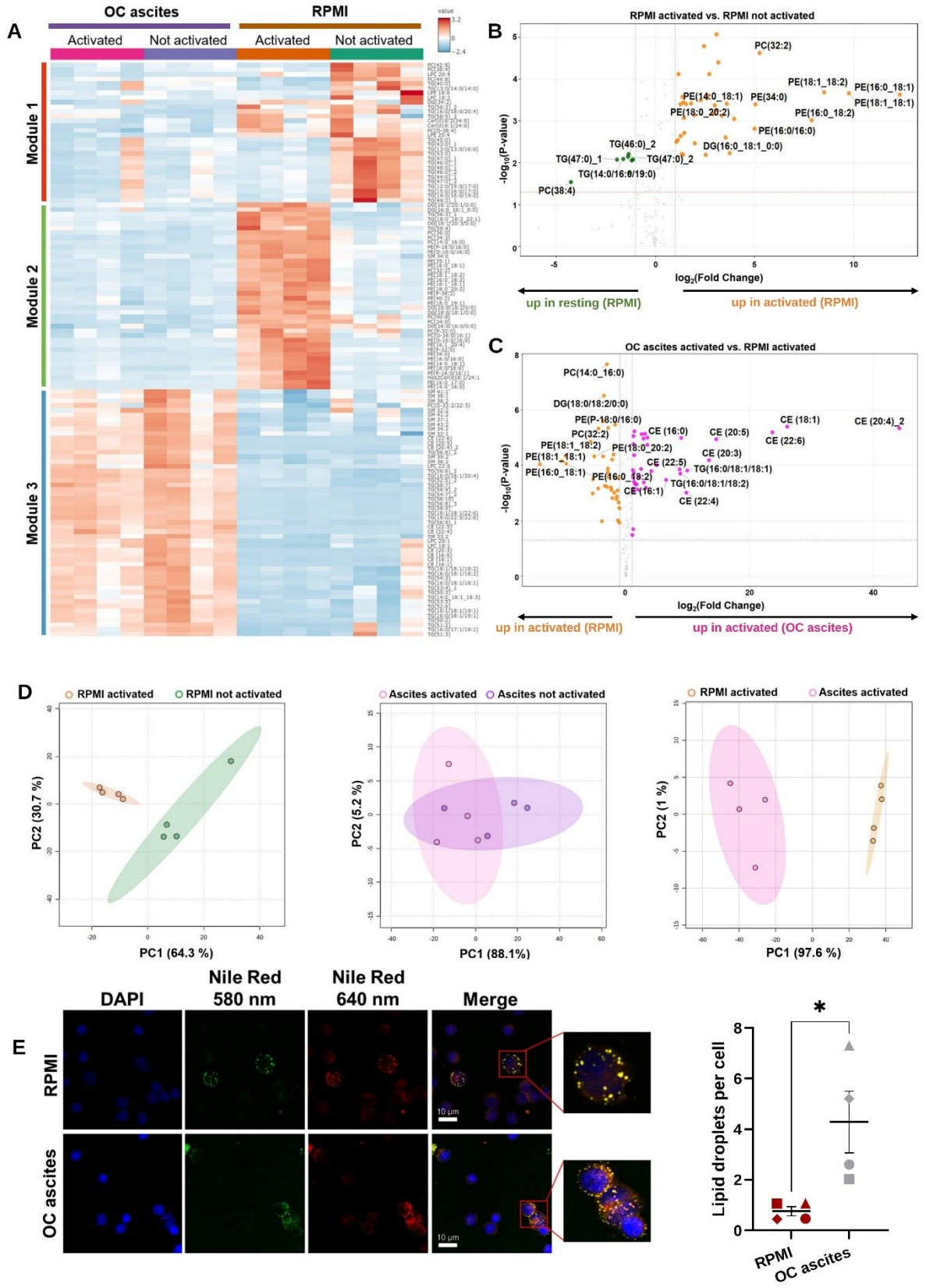


1000

1001

Figure 3. OC ascites suppresses TCR-driven signal transduction and TCR trafficking. (A) IRF4 protein expression (gMFI) in $CD8^+$ T cells activated for 16 h with TAE beads (2:1) in RPMI, LC ascites, or OC ascites, assessed by intracellular flow cytometry. Representative histograms (left) and summary data (right) are shown. Data represent mean ± SEM from n = 5 HD. Repeated-measures one-way ANOVA. *P < 0.05. (B–D) $CD8^+$ T cells obtained from HD PBMC were transfected with scrambled control (scr) or IRF4-targeting (siIRF4) siRNA by electroporation and stimulated with TAE beads (2:1) for 16 h in RPMI. (B) Intracellular IRF4 protein expression (gMFI) confirming knockdown efficiency. (C) Frequency of eFluor670-diluting proliferating cells. (D) Frequency of $CD25^+CD69^+$ activated cells. Data represent mean ± SEM from n = 4 HD. Paired *t*-test. *P < 0.05, **P < 0.01. (E) Schematic illustration of the proximal TCR signaling cascade upon antigen recognition, showing key signaling molecules including Lck, ZAP70, PLCγ1, and downstream MAP kinase and NF-κB pathways, Created in BioRender. Jouria, A. (2027) https://BioRender.com/uzlaq0l and adapted from Janeway's Immunobiology (10th edition). (F) Kinetic analysis of proximal TCR signaling in $CD8^+$ T cells stimulated with anti-CD3 and $F(ab')_2$ crosslinking in RPMI or OC ascites. Phosphorylation levels (gMFI) of pLck-Tyr394, pZAP70-pY292, pPLCγ1-pY783, and pERK1/2-pT202/pY204 were assessed by intracellular flow cytometry at 0, 0.5, 1, 2, and 5 minutes post-crosslinking (n = 3 HD). Two-way ANOVA. *P* values are indicated for each phosphorylation event. (G) TCR α/β surface expression (gMFI) on $CD8^+$ T cells activated in RPMI or OC ascites, assessed after isolation (baseline), after 16 h activation, and following 6 h and 24 h of resting (n = 3 HD). Two-way ANOVA. *P*-value is indicated for the last measurement time point.

Figure 4

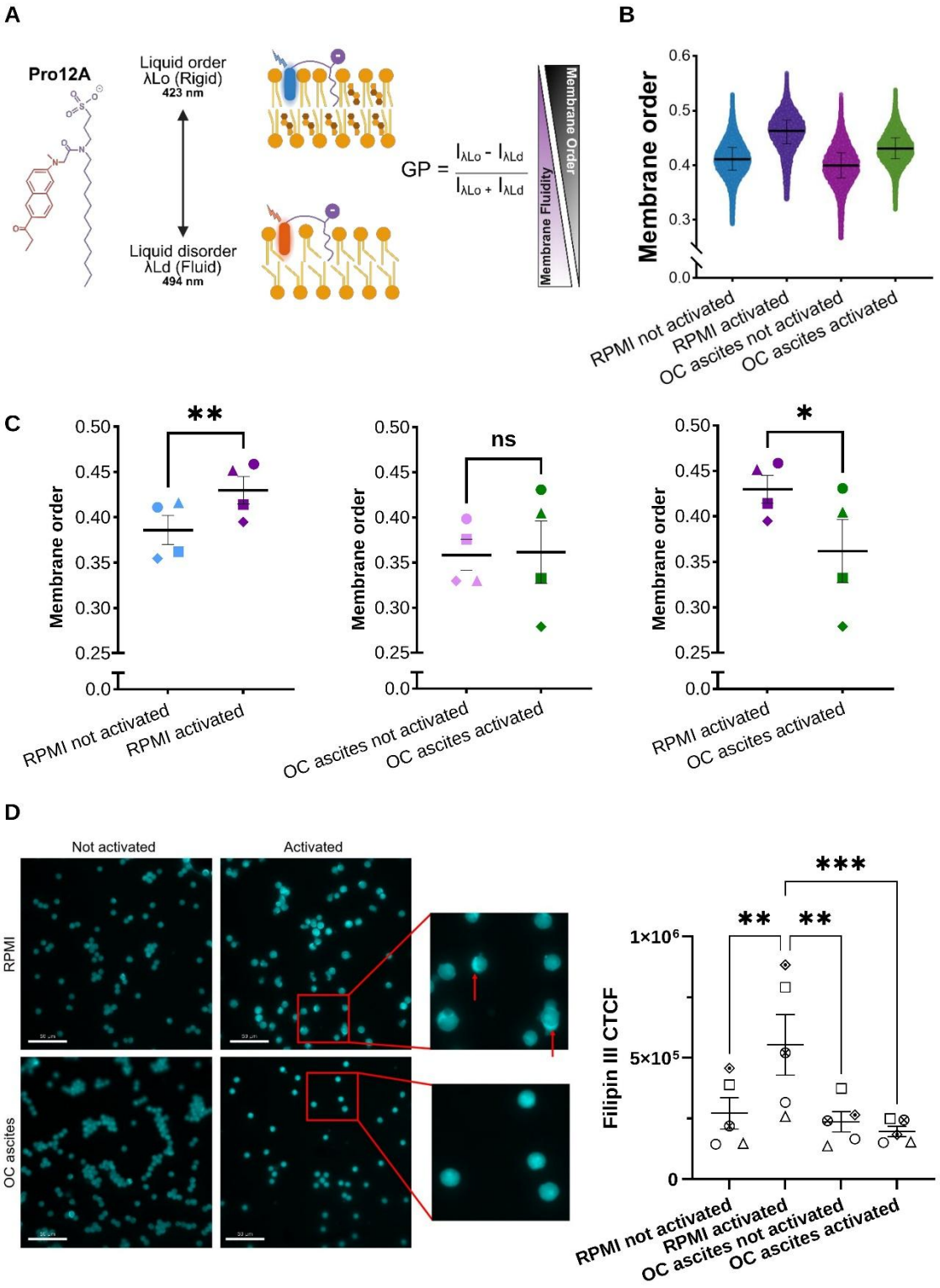


1023

1024

Figure 4. OC ascites alters lipid remodeling and promotes lipid droplet generation. (A) Heatmap of differentially abundant lipid species identified by untargeted lipidomics in $CD8^+$ T cells across four conditions: RPMI non-activated, RPMI activated (16 h with TAE beads, 2:1), OC ascites non-activated and OC ascites activated (16 h with TAE beads 2:1), classified into three modules based on their differential abundance patterns (n = 4 HD). (B–C) Volcano plots displaying differentially abundant lipid species in $CD8^+$ T cells (B) activated versus non-activated in RPMI, or (C) activated in RPMI versus OC ascites. The horizontal dashed red line indicates the significance threshold ($P = 0.05$, unpaired Student's *t*-test), vertical dashed lines indicate the fold-change cutoff (±1). Lipid species enriched in each condition are color-coded and indicated on the x-axis. (D) Principal component analysis (PCA) of the untargeted lipidomics dataset showing separation of lipids detected in $CD8^+$ T cells RPMI-activated vs. non-activated (left), OC ascites activated vs. non-activated (middle), and activated in RPMI vs. OC ascites (right) (n = 4 HD). Ellipses represent 95% confidence intervals. (E) Representative confocal microscopy images of $CD8^+$ T cells activated in RPMI or OC ascites, stained with Nile Red to visualize intracellular lipid droplets. Nile Red emission at 580 nm detects neutral lipids (cholesterol esters and triglycerides, shown in yellow/green) within lipid droplets, while emission at 640 nm detects polar lipids including phospholipids (shown in red). Nuclei were counterstained with DAPI. Scale bar, 10 µm. Dot plot show lipid droplets per cell (total LDs / total cells per donor); each symbol represents one donor (n = 4 HD). Ratio paired *t*-test. $*P < 0.05$.

Figure 5



1045

1046

Figure 5. OC-ascites alters plasma membrane order and restricts intracellular cholesterol accumulation. (A) Schematic illustration of the generalized polarization (GP) using the Pro12A membrane probe. GP is calculated from the emission intensities at 423 nm (liquid-ordered, rigid phase) and 494 nm (liquid-disordered, fluid phase), providing a quantitative measure of plasma membrane order Created in BioRender. Jouria, A. (2026) https://BioRender.com/lxp9lqr. (B) Representative violin plots showing membrane order (GP values) of $CD8^+$ T cells from one donor across four conditions: RPMI non-activated, RPMI activated (16 h with TAE beads 2:1), OC ascites non-activated, and OC ascites activated (16 h with TAE beads 2:1). Horizontal lines indicate the median and interquartile range. (C) Summary data showing membrane order (GP values) comparing RPMI non-activated vs. activated (left), OC ascites non-activated vs. activated (middle), and RPMI activated vs. OC ascites activated (right) $CD8^+$ T cells activated as in Fig. 1 (n = 4 HD). Paired *t*-test. $*P < 0.05$, $**P < 0.01$, ns = not significant. (D) Representative confocal microscopy images of $CD8^+$ T cells stained with Filipin III to visualize free cholesterol under non-activated and activated (16 h with TAE beads 2:1) conditions in RPMI or OC ascites. Scale bar: 50 µm. The graph shows corrected total cell fluorescence (CTCF) quantification of Filipin III signal across four conditions (n = 5 HD). Statistical analysis: repeated measures (RM) one-way ANOVA. $**P < 0.01$, $***P < 0.001$. Data in (C, D) are presented as mean ± SEM; data in (B) show median and interquartile range. Each point represents an individual donor.

Figure 6

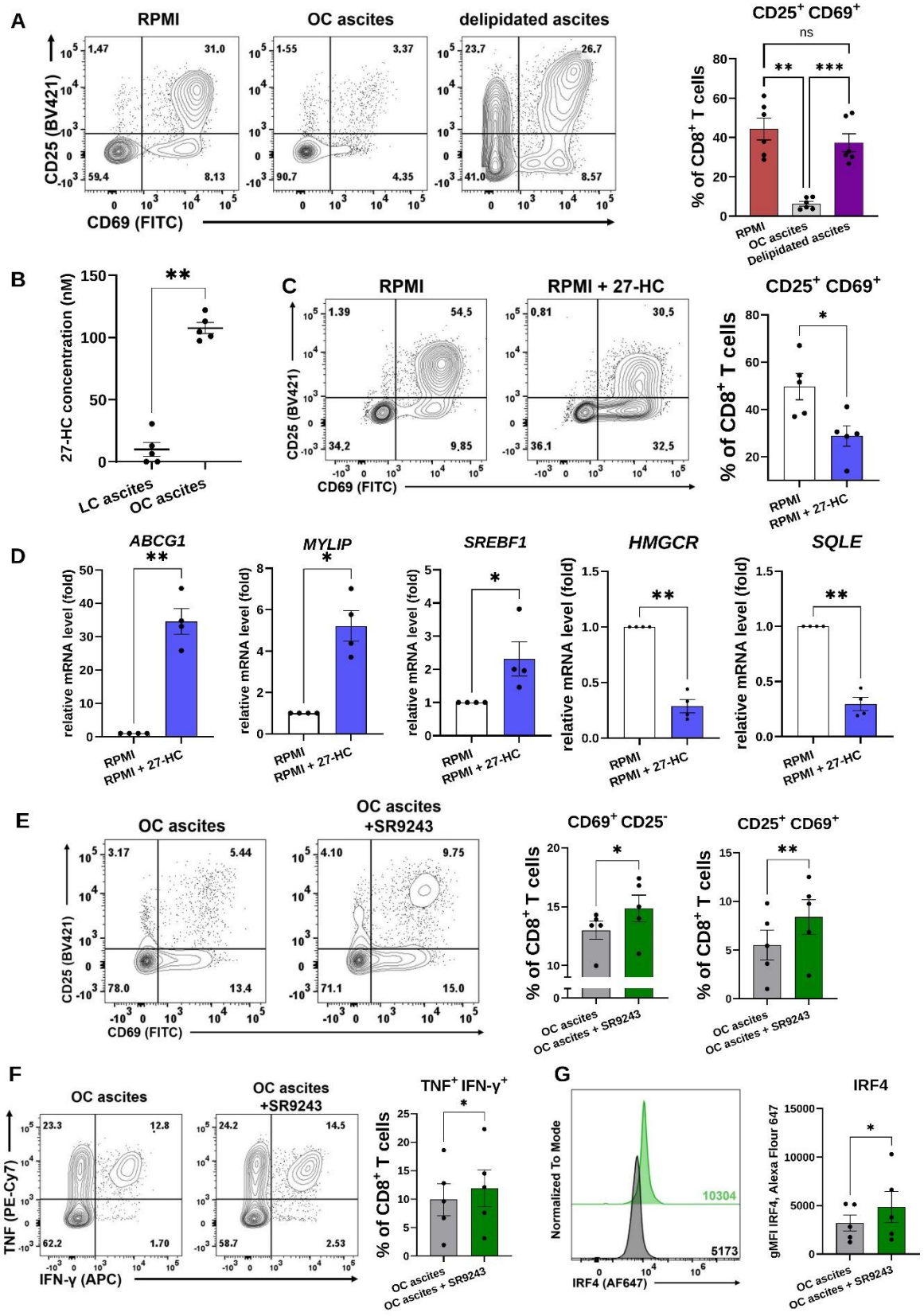

A
RPMI
OC ascites
delipidated ascites
CD25 (BV421)
CD69 (FITC)
1.47
31.0
59.4
8.13
1.55
3.37
90.7
4.35
23.7
26.7
41.0
8.57
CD25+ CD69+
ns
**
***
% of CD8+ T cells
RPMI
OC ascites
Delipidated ascites
B
**
27-HC concentration (nM)
LC ascites
OC ascites
C
RPMI
RPMI + 27-HC
1.39
54.5
34.2
9.85
0.81
30.5
36.1
32.5
CD25+ CD69+
*
% of CD8+ T cells
RPMI
RPMI + 27-HC
D
ABCG1
MYLIP
SREBF1
HMGCR
SQLE
relative mRNA level (fold)
RPMI
RPMI + 27-HC
E
OC ascites
OC ascites +SR9243
3.17
5.44
78.0
13.4
4.10
9.75
71.1
15.0
CD69+ CD25-
CD25+ CD69+
% of CD8+ T cells
OC ascites
OC ascites + SR9243
F
OC ascites
OC ascites +SR9243
TNF (PE-Cy7)
IFN-γ (APC)
23.3
12.8
62.2
1.70
24.2
14.5
58.7
2.53
TNF+ IFN-γ+
G
Normalized To Mode
IRF4 (AF647)
10304
5173
IRF4
gMFI IRF4, Alexa Flour 647

Figure 6. 27-HC/LXRβ signaling axis contributes to the impaired $CD8^+$ T cell activation in OC ascites. (A) HD $CD8^+$ T cells were activated with TAE beads (2:1) for 16 h in RPMI, OC ascites, or delipidated OC ascites. Representative flow cytometry dot plots and a summary bar graph show frequencies of $CD25^+CD69^+$ $CD8^+$ T cells (n = 6 HD). Repeated-measures one-way ANOVA. $^{**}P < 0.01$, $^{***}P < 0.001$, ns = not significant. (B) Targeted mass spectrometry quantification of 27-HC in OC ascites versus LC ascites. n = 5 per group. Unpaired t-test. $^{**}P < 0.01$. (C–D) HD $CD8^+$ T cells were stimulated with TAE beads (2:1) in RPMI ± 27-HC (10 μM) for 16 h. (C) Frequency of $CD25^+CD69^+$ activated $CD8^+$ T cells. (D) Relative mRNA expression of *ABCG1, MYLIP, SREBF1, HMGCR*, and *SQLE*, normalized to 18S rRNA and the RPMI condition (n = 4-5 HD). Paired t-test. $^{*}P < 0.05$. (E–G) HD $CD8^+$ T cells were activated with TAE beads (2:1) in OC ascites ± SR9243 (50 μM) for 16 h. (E) Representative flow cytometry dot plots and summary data showing frequencies of $CD69^+CD25^-$ and $CD25^+CD69^+$ $CD8^+$ T cells. (F) Frequency of $TNF^+IFN\gamma^+$ double-positive $CD8^+$ T cells. (G) Intracellular IRF4 protein expression (gMFI); representative histogram and paired summary data shown (n = 5 HD). Paired t-test. $^{*}P < 0.05$, $^{**}P < 0.01$. Data are presented as mean ± SEM. Each data point represents an independent donor.

Supplementary Files

This is a list of supplementary files associated with this preprint. Click to download.

- TableS6.LipidspeciesdetectedinCD8XXXTcellsactivatedinRPMIorOCascites.xlsx
- SupplementaryInformationJouriaetal.docx
- TableS4.Normalizedgeneexpression.xlsx
- TableS7.LipidspeciesincreasedinOCascitescomparedwithRPMI.xlsx
- SupplementaryInformationJouriaetal.docx
- UnprocessedoriginalimagesFig4Eand5D.pdf